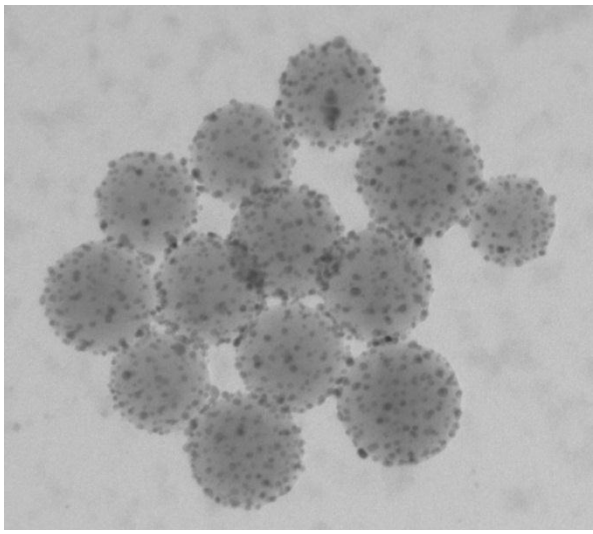

Preparation and Characterization of Novel Luminescent Nanoparticles for Biodiagnosis Applications

Diogo Manuel Rodrigues Ferreirinha
Mestrado em Bioquímica
Departamento de Química e Bioquímica
2012

Orientador
Peter Eaton, Investigador Auxiliar, Faculdade de Ciências

Coorientador
Eulália Pereira, Professora Auxiliar, Faculdade de Ciências

U.PORTO

FACULDADE DE CIÊNCIAS
UNIVERSIDADE DO PORTO

Todas as correções determinadas pelo júri, e só essas, foram efetuadas.

O Presidente do Júri,

Porto, _____/_____/_____

Acknowledgements

To Dr. Peter Eaton, for guiding me through the challenges posed by the present work.

To Dr. Eulália Pereira, for teaching me about many of the theoretical concepts and experimental tools used in this work.

To Dr. Craig Medforth, for his invaluable aid in the nuclear magnetic resonance experiments described in the present work.

To Dr. Salete Balula, for aiding me in understanding silica chemistry.

To Dr. Cristina Neves, for teaching me how to work in a chemistry laboratory with the utmost rigorousness and efficiency.

To Dr. Pedro Quaresma, for his important contribution in planning and understanding some of the experiments described in this work, and for his witty humorous remarks.

To Dr. Leonor Ricardo, for sharing her knowledge and experience in working with gold nanoparticles, and for her sincere and friendly mood.

To Dr. Ana Lobão, for sharing her views and experience in Nanochemistry.

To Dr. Carla Queirós, for helping me through finding many of the materials used in the present work.

To Dr. Ana Cristina Freire, for introducing me to the fascinating science of Nanochemistry.

To all my other colleagues in the Inorganic Chemistry group, for the great work environment I have found while working with you.

To all my friends, for sharing what we live.

To Marlene, for being there.

And last but not least, to my mother, to Zé, to my brother and to my cat Che, for being my family.

Resumo

A síntese de nanopartículas de sílica com rodamina isotiocianato (RITC-SiNPs) foi abordada no presente trabalho com o intuito de fornecer uma plataforma eficiente com fluorescência para a criação de dois novos biosensores de DNA. O primeiro biosensor criado consiste numa versão de RITC-SiNPs funcionalizada com o epoxisilano 3-glicidiloxipropil trimetoxisilano (GPTMS) para servir como uma molécula de ligação para sondas tioladas de ssDNA, resultando assim num biosensor fluorescente de DNA. O segundo biosensor a ser criado consiste numa versão de RITC-SiNPs decorada com ouro, que combina fluorescência com absorção plasmónica para a deteção de sequências específicas de DNA. A preparação da superfície das nanopartículas (NPs) para decoração com ouro por meio de uma metodologia de deposição-precipitação foi feita por funcionalização com o aminosilano 3-aminopropil trietoxisilano (APTES), bem como por uma estratégia alternativa que engloba a cobertura da superfície das NPs com camadas singulares e múltiplas constituídas pelos polímeros hidrocloreto de polialilamina (PAH) e poliestirenossulfonato (PSS).

Foi demonstrado que as RITC-SiNPs fornecem um material de base eficiente para a criação de biosensores devido à sua fotoestabilidade, boa dispersão de tamanho e uma química de superfície versátil para posteriores modificações. A funcionalização com GPTMS forneceu também bons resultados relativamente à preservação de fluorescência das NPs, estabilidade do grupo epóxido e forte interação com a superfície das NPs. No entanto, a funcionalização com APTES resultou numa redução significativa da fluorescência das NPs, sendo que esta diminuição é provavelmente devida à presença de APTES auto-polimerizado em solução. A estratégia alternativa de cobrir a superfície das NPs com uma camada de PAH foi bem sucedida na preservação da fluorescência das NPs, enquanto que o uso de camadas múltiplas de PAH e PSS resultou na redução significativa de fluorescência. A decoração com ouro após ambos os métodos de preparação da superfície das NPs foi feita com sucesso, mas observou-se uma redução drástica de fluorescência das NPs que se deve provavelmente à extinção de fluorescência ou *quenching* pelo ouro. Estes resultados indicam que a funcionalização das RITC-SiNPs com GPTMS foi eficiente, mas a combinação da absorção por ressonância plasmónica com a fluorescência das RITC-SiNPs requer estudos adicionais de forma a prevenir fenómenos de *quenching*.

Palavras-chave: Nanopartículas multifuncionais de sílica, fluorescência, decoração com ouro, funcionalização com silanos, funcionalização com polielectrólitos

Abstract

The synthesis of rhodamine isothiocyanate doped silica nanoparticles (RITC-SiNPs) was studied in the present work in order to provide an efficient fluorescence capable platform for the design of two novel sequence-specific DNA biosensors. The first biosensor to be designed consists in a version of RITC-SiNPs functionalized with the epoxysilane 3-glycidyloxypropyltrimethoxisilane (GPTMS) to act as a linker molecule for the attachment of thiolated ssDNA probes, thus resulting in a fluorescent DNA biosensor. The second biosensor intended for design is a gold decorated version of RITC-SiNPs that combines fluorescence and plasmonic-based absorption for the detection of specific gene sequences. The preparation of the nanoparticle (NP) surface for gold decoration by a deposition-precipitation method was carried by functionalization with the aminosilane 3-aminopropyltriethoxysilane (APTES) and also by using an alternative strategy consisting in capping the surface of the NPs with single and multiple layers of the polyelectrolytes polyallylamine hydrochloride (PAH) and polystyrene sulfonate (PSS).

It has been shown that the RITC-SiNPs provide a solid base material for the design of biosensors, coupling photostability with good size dispersion and a versatile surface chemistry for further functionalization. The functionalization with GPTMS has also yielded good results in terms of the preservation of RITC-derived fluorescence, stability of the epoxide ring for further modification, and strong interaction with the surface of the NPs. However, the APTES functionalization of the NPs resulted in severe reduction of the NP fluorescence, which was found to be likely related to the presence of self-polymerized APTES in solution. The alternative strategy of using single layer coating of the NPs with PAH was successful in preserving NP fluorescence, while the multiple layer coating with PAH and PSS resulted in significant reduction of NP fluorescence. Gold decoration after both methods of surface preparation was successful, but a drastic reduction in NP fluorescence likely due to the extinction of fluorescence or quenching by gold was consistent. These results indicate that the GPTMS functionalization of the RITC-SiNPs was efficient, but combining the plasmonic-based absorption of gold with the fluorescence of the RITC-SiNPs still requires further study towards preventing the extinction of the fluorescence.

Keywords: Multifunctional silica nanoparticles, fluorescence, gold decoration, functionalization with silanes, functionalization with polyelectrolytes

Index

Figure index

Table index

Abbreviations and symbols

AFM – Atomic force microscopy

APTES – 3-aminopropyltriethoxysilane

DLS – Dynamic light scattering

DNA – Deoxyribonucleic acid

DRIFTS – Diffuse reflectance infrared Fourier transform spectroscopy

DP – Deposition-precipitation

FTIR - Fourier transform infrared spectroscopy

GPTMS – 3-glycidyloxypropyltrimethoxysilane

NMR – Nuclear magnetic resonance

NP - Nanoparticle

PAH – Polyallylamine hydrochloride

PCR – Polymerase chain reaction

PSS – Polystyrene sulfonate

RITC - Rhodamine-B isothiocyanate

RITC-SiNP – Rhodamine-B isothiocyanate-doped silica nanoparticle

TEM – Transmission electron microscopy

UV-Vis – Ultraviolet-visible

Chapter I

Introduction

1. Nanoparticles as biosensors

A biosensor may be generally defined as a sensor that couples a biological recognition entity with a physical element that acts as a transducer for the recognition event, although many definitions can be found according to the specific field of application, since the detection of specific analytes that are known to interact with biomolecules encompasses a wide array of applications in various fields such as medicine, agriculture, biotechnology and environmental sciences, as well as in the military and biochemical terrorism detection and prevention [1]. Despite these terminological differences, there is a consensus that a biosensor comprises two distinct elements: a biologically-derived element and a sensor element. The basic concepts of a biosensor's functionality are illustrated in Figure 1, where a specific analyte interacts with the biological element (such as an enzyme or a nucleic acid) which in turn recognizes the analyte and causes a change in the transducer component, thus resulting in the generation of a signal [2].

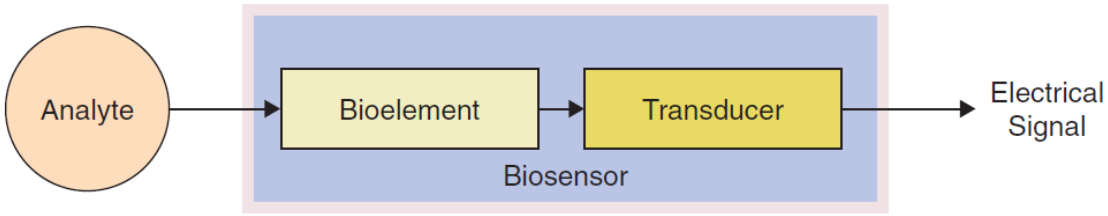

Figure 1- General schematic representation of a biosensor (reproduced from reference [3]).

As shown in Figure 2, biosensors can be applied in various fields due to abundant market potential, but their effective commercial adoption is hampered by current technological limitations. For example, currently available biosensing techniques for DNA detection comprise the need for sample amplification by polymerase chain reaction (PCR) in order to provide the necessary amounts for further analysis by commercially available techniques such as gel electrophoresis, radioactive or fluorescence labeling. These detection techniques are known for their proneness to false positives and false negatives, as well as being time consuming and involving significant costs [4]. To counteract this limitation, biosensing systems such as force amplified biological sensors (FABS), bead array counter (BARC) and force differentiation assays (FDA) were developed in order to

provide reliable measurements in a single easy operation. In these systems, magnetic microbeads are used to pull DNA-DNA or antibody-antigen bonds with a known force, and the detachment strengths of the bonds are observed with a micromechanical sensor (FABS) or a magnetoresistive sensor (BARC). In addition, the implementation of micro electromechanical systems (MEMS) has made the fabrication of portable battery operated biosensors with an integrated PCR capability possible, thus providing increased speed, efficiency in number of DNA copies produced, ability to use small volumes and reduced costs. However, these biosensors are still significantly limited in terms of sensitivity [3].

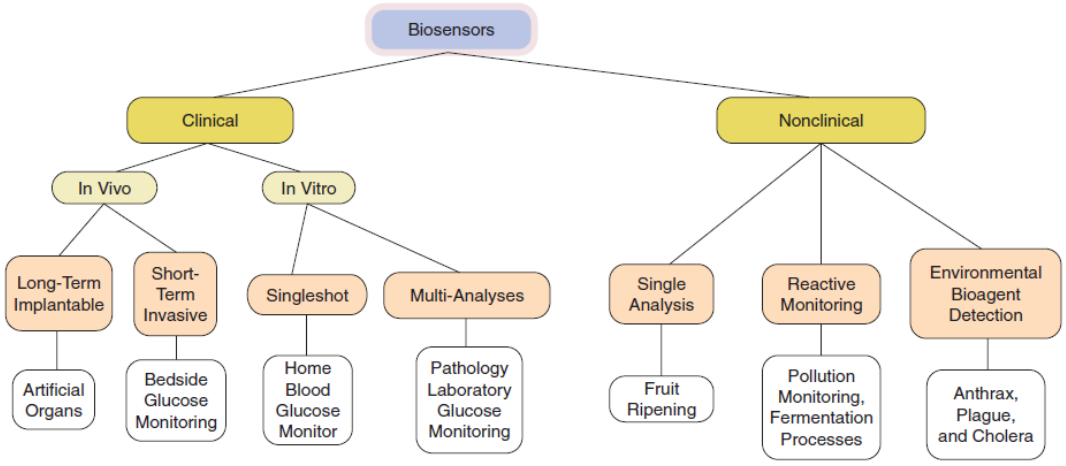

Figure 2 – Potential fields of application for biosensing (reproduced from reference [4]).

In order to surpass the limitations of the currently available biosensing techniques, new approaches to biosensing are being developed, and many of these new approaches are based on nanotechnological platforms. In general consensus, nanotechnology comprises devices and processes with scales below 100 nm. At this scale, the manifestation of physical processes is significantly different from processes at greater scales due to quantum effects such as in quantum dots and tunnel junctions. Furthermore, surface to volume ratios are larger, thus potentiating the functionality of sensors that interact with analytes on their surface. Also, many of the analyte molecules of interest have nanoscale dimensions, and developing nanobiosensors allows detecting the analytes with technologies that are controllable at this scale, thus opening up the possibility to tune the nanobiosensors towards more efficient approaches for detecting their respective target analytes [4].

The functionality of nanobiosensors can be explained by the thoughtful assembly of an inorganic component (usually as the core of the nanobiosensor) with specific biomolecules that will fulfill the role of interacting with the analyte of interest. The core component may also comprise further subcomponents that may be inorganic or organic. In general, the design of nanobiosensors aims to couple the physical properties of the core components that allow the generation of signals with the recognizing and interaction capabilities provided by the biological components [5]. However, in order to ensure an efficient functionality of the nanobiosensor as a whole, additional building iterations may be used, whether organic or inorganic, as illustrated in Figure 3.

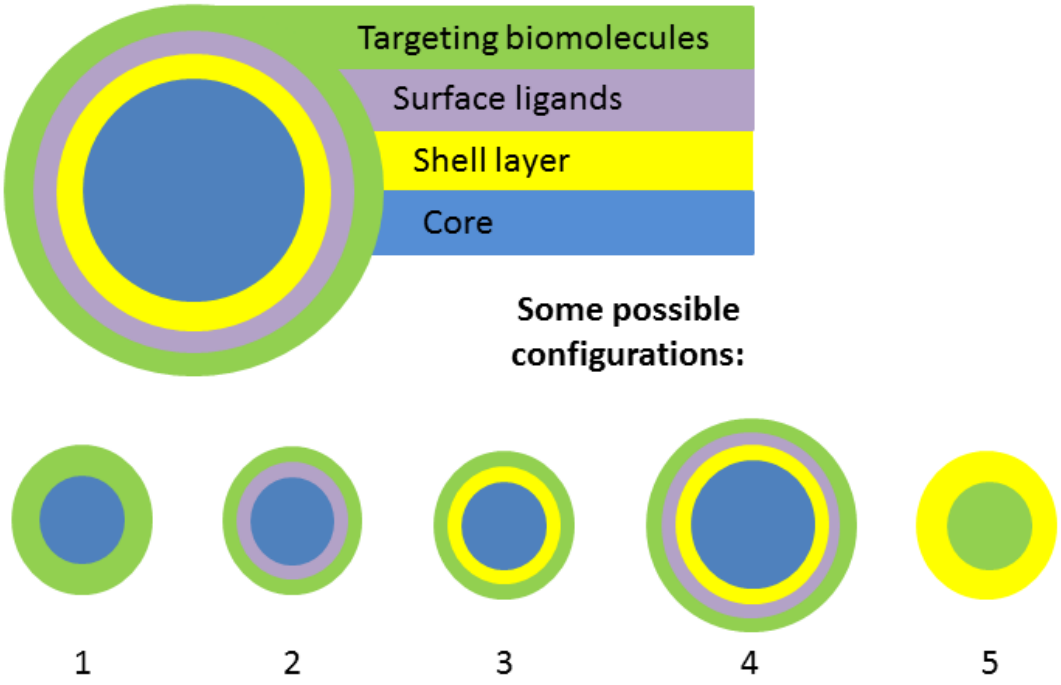

Figure 3 – Overview of commonly used structural frameworks for nanobiosensors.

One of the chief goals in designing nanobiosensors is to attain significant increases in overall sensitivity towards target analytes, and in this context, sensitivity may be defined in various distinct ways. In order to evaluate the effectiveness of detection of a specific analyte by a given sensor, one of the main parameters that is usually taken into account is the internal sensitivity of a sensor. This parameter consists of the ratio between the sensor's output signal and the change in the property of the sensor that results in the output signal, assuming that this change is due to the variable interaction of the target analyte with the sensor. More frequently, the interacting analyte quantity of interest is expressed in concentration of analyte instead of total mass or number of molecules, thus taking into account not only the sensitivity of the transducer itself but also the total

exposed area of the sensor and the interaction kinetics between the sensor and the analyte [6]. Another usual way of defining sensitivity is to relate it to a minimum detectable quantity of analyte that can be resolved above a background signal, known as limit of determination (LOD). Until now, various nanobiosensors have been developed towards increased sensitivity as understood according to the aforementioned parameters [7] [8], resulting in a continuous interest in developing novel nanobiosensors for the detection of a wider array of analytes that are shown to be undetectable by commercially available techniques without added costs and time in extraction and purification methodologies. In this context, the effective interaction between the core components of the nanobiosensor and the probe molecule that will recognize and interact with the analyte is the main factor for attaining optimal sensitivity.

Another desired property in biosensors is the specificity, defined as the ability to distinguish the target analyte from other materials present in the sample [4]. The use of nanobiosensors may also allow increased specificity towards analytes of interest by more effectively exploiting complex or specific interactions such as antibody-antigen, nucleic acid hybridization, enzyme-substrate interactions, etc. In this context, the techniques used to obtain specific interactions between the sensor and the analyte depend mainly on the sensor's surface chemistry and also on the building strategy chosen. One of the methods used, despite being a simplistic approach and presenting fewer possibilities for differentiation in the interaction with the various components of a given sample, is physical adsorption [9]. Physical adsorption comprises the exposure of the sensor's surface to the target analyte and subsequent non-covalent interaction of the analyte with the exposed surface of the sensor. One example of the use of this method of interaction in nanobiosensors is the nonspecific adsorption of proteins and DNA to the surface of carbon nanotubes (CNTs) [10]. Physical adsorption is also commonly used in structural building of probe-nanoparticle complexes for further detection of specific molecules, and one example is the adsorption of polyelectrolytes such as polyallylamine hydrochloride (PAH) or polystyrene sulfonate (PSS) to the surface of nanobiosensors [11]. This is one of the methodologies used in this work, although not in a sensor-analyte interaction perspective but rather with the objective of building the necessary infrastructure for probe immobilization. In this context, another approach is to rely on covalent bonding between the probe and the nanobiosensor's surface, such as in the case of silica surfaces that present hydroxyl end groups –Si-OH, commonly known as silanol groups.

These groups allow binding various types of organofuctional alkoxysilanes that can be used to covalently bind probe molecules such as DNA by exposing functional groups such

as amines or epoxides [12], thus providing various possibilities for achieving specific probe-analyte interactions.

2. Nanobiosensors in gene detection applications

The increasing advances in understanding the structure and functionality of nucleic acid molecules have made sequence-specific DNA detection an important factor in many fields such as medical genetics, pathogen detection, food technology, environmental sciences, gene therapy, drug research and development, etc. [13-16] Therefore, the development of more simple, rapid, user-friendly and effective methods for the detection of specific DNA sequences is paramount in order to meet these needs. More specifically, advances in DNA detection technology are essential to the progress of medicine, since being able to identify and detect gene sequences can provide detailed knowledge of disease pathways, presence of pathogens and patients' conditions. However, the majority of the tests currently available is slow, require significant amounts of sample material and may lead to false positive or negative results [4]. These limitations motivate the development of improved detection techniques aiming for increased reliability, quickness, cost effectiveness and range of detectable samples [17]. The state-of-the-art technologies currently available for genetic diagnosis comprise sample amplification by polymerase chain reaction (PCR) followed by commercially available detection methods such as gel electrophoresis or use of fluorescent or radioactive labels, among others. PCR comprises amplification of the signal by selectively replicating the target nucleotide sequences due to the use of appropriate primers. Therefore, these techniques require significant and intensive sample preparation, thus resulting in potential errors in diagnosis and increased costs, and the sensitivity of the assays significantly limits detection capability [18].

In recent years, the design of novel DNA biosensors based on nucleic acid hybridization has been pursued. DNA biosensors generally comprise a single-stranded oligonucleotide probe integrated in a transducing microsystem that can be of various types, such as optical, thermometric, piezoelectric, magnetic, electrochemical or micromechanical. These biosensors aim to generate discrete or continuous signals according to the concentration of the target DNA sequence. In comparison with the commercially available DNA detection methodologies, DNA biosensors allow for

increased specificity, speed and ease-of-use while reducing costs. However, the low concentration of analytes in various samples is a limiting factor for these biosensors [19].

In this context, nanotechnology has triggered the research and development of DNA biosensors that operate at the nanoscale, thus allowing the selective control of their properties by means of the size, morphology and composition of the nanoparticles. Until now, these novel DNA nanobiosensors have been developed using nano-materials such as gold nanoparticles, CdS quantum dots, Si nanowires, CNTs, among others [19]. These materials allow the design of platforms for DNA attachment and signal amplifiers for hybridization, therefore allowing significant increases in detection sensitivity [19].

3. Hybrid and multifunctional nanoparticles

Recent advances in nanotechnology and biotechnology have resulted in the development of multifunctional nanoparticles with the initial intent of enabling target-specific delivery of imaging or therapeutic agents for biomedical applications. Currently, the use of multifunctional nanoparticles for the detection of specific gene sequences is found to be effectively applied in the fields of multimodal imaging and theragnosis (integration of therapy with diagnosis) [20].

The development of multifunctionality in nanomaterials is related to the ability to structurally modify these materials with specific moieties that are selected in order to provide the intended functionalities while conferring efficient integration of the various components in one material [21]. In a broad definition, hybrid nanoparticles can be defined as nanomaterials that include two or more moieties blended on the molecular scale. The possible interactions between the various moieties range from weak interactions such as van der Waals, hydrogen bonding or weak electrostatic interactions to strong interactions such as covalent bonding, coordinative interactions and ionic interactions. Furthermore, hybrid nanomaterials can be distinguished according to their structural properties. For example, an organic moiety such as 3-aminopropyltrimethoxysilane (APTES) acts as a network functionalization compound by containing a functional group, which in this case consists of the three ethoxy groups that allow its attachment to an inorganic network (i. e. silica network), while providing an amino group that may be used for further modification

of the hybrid material [22]. In contrast, an organic moiety consisting of compounds such as phenyltrialkoxysilanes acts as a network modifying compound by modifying silica networks in sol-gel processes via reaction of the alkoxysilane groups without providing functional groups for further chemical reactions.

Various DNA detection biosensors consisting of hybrid nanoparticles have been developed in recent years, and some types of nanomaterials such as quantum dots, gold, iron oxide and silica nanoparticles have been used as inorganic platforms [23]. These different materials provide specific advantages according to the intended end use. For example, iron oxide nanoparticles allow the use of magnetism for sample separation, while some possess inherent limitations, such as in the case of quantum dots, most of which exhibit significant toxicity.

4. Dye-doped fluorescent silica nanoparticles

The use of fluorescence for the detection of specific gene sequences presents many advantages such as sensitivity, simplicity and diversity while providing real time *in-situ* information [24]. DNA detection approaches that combine the use of fluorescence with the use of nanoparticles have been shown to provide further advantages such as increased fluorescence, high photostability and larger Stokes shifts in comparison with other methodologies that involve the use of organic fluorescent dyes, and these advantages enable their use in single molecule imaging, high-throughput assays and long-term real-time tracking of analytes *in vivo* [25]. In this context, the nanoscale integration of organic fluorescent dyes by encapsulation within a silica network offers several advantages, allowing to counter some of their main disadvantages in biological applications such as hydrophobicity or proneness to quenching and photobleaching. Silica encapsulation has also been shown to improve detection limits in biosensing by preventing interactions between the fluorophore and the buffer [26]. Furthermore, silica chemistry is currently well-established, allowing effective chemical modifications that pave the way for modifying the nanoparticles in order to optimize their targeting capabilities and interactions with their environment of use [27].

The synthesis of dye-doped silica nanoparticles can be achieved by two distinct methodologies: the Stöber method [28] and the reverse microemulsion method developed by Bagwe *et al.* [29]. The Stöber method allows the synthesis of dye-doped silica nanoparticles through condensation and hydrolysis reactions by mixing a silica precursor such as TEOS into absolute ethanol in the presence of ammonium hydroxide and the fluorescent dye. This method is regarded as simple and effective, albeit presenting several disadvantages, such as a significant increase of size polydispersity associated with decreasing the size of the nanoparticles, as well as a poor encapsulation yield of the fluorescent dye due to its dependence towards the absorption force between the dye and the silica precursor used [30]. In contrast, the reverse microemulsion method allows the effective retention of dye in the silica nanoparticles by using water soluble dyes in size controllable nanoreactors consisting of reverse micelles within which the formation of the silica network will take place. Modulation of nanoreactor size can in turn be achieved by adjusting parameters such as reaction time, oil to water ratio and choice of surfactant, co-surfactant or hydrolysis reagent [31]. This method has been shown to successfully yield hydrophilic and highly monodisperse nanoparticles; however, the problem of dye leakage is still observable; therefore, the choice of dye for further encapsulation remains as a main factor by influencing both the loading efficiency and the relative amount of leaked dye [32].

In this work the dye chosen for encapsulation was rhodamine B isothiocyanate (RITC), which is a hydrophilic dye that presents isomerism. It is known that the encapsulation of hydrophilic dyes can be achieved by the single use of TEOS as a silica precursor [30]. It is also known that the stability of the interactions between the encapsulated dyes and the silica network is substantially different among the distinct isomers [30]. In the present work, a combination of mixed isomers of RITC was added in excess to account for this factor.

The encapsulation of organic dyes does not significantly alter their emission and excitation spectra in comparison with the free dye, although shifting of peaks may occur due to the preferential retention or locking of certain isomerisms or to the affinity between the dye and the silica network, in which case the chosen silica precursor may be specifically selected in order to avoid undesirable peak shifts [30]. Most importantly, the encapsulation of fluorescent dyes should prevent quenching or photobleaching of the dyes, while providing a silica surface that may be used for further modification of the silica nanoparticles.

In the context of the present work, the initial goal was to synthesize RITC-doped silica nanoparticles (RITC-SiNPs), and to further functionalize their surface in order to

obtain two novel DNA biosensors: one with fluorescence emission capability (FL-SiNPs), and another with both fluorescence and plasmonic-based absorbance (FL-Au-SiNPs) conferred to it by a surface decoration with gold nanoclusters (Figure 4).

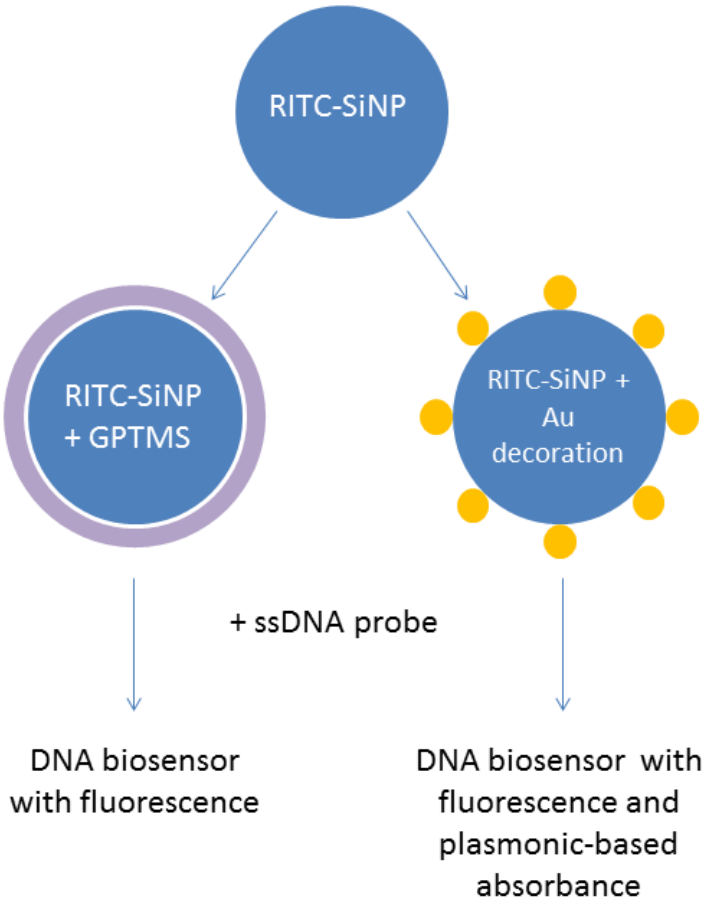

Figure 4 – Biosensors intended for synthesis in the present work.

In the first case, the chosen functionalization methodology was to modify the surface of the nanoparticles with 3-glycidyloxypropyltrimethoxysilane (GPTMS), a silane that contains a trimethoxy group to covalently bind to the silica network through a multi-step reaction (as described in Figure 5) with the silanol groups at the surface of the RITC-SiNPs, while providing an epoxy group that is intended to react with thiolated oligonucleotides that can act as probes for the detection of target DNA.

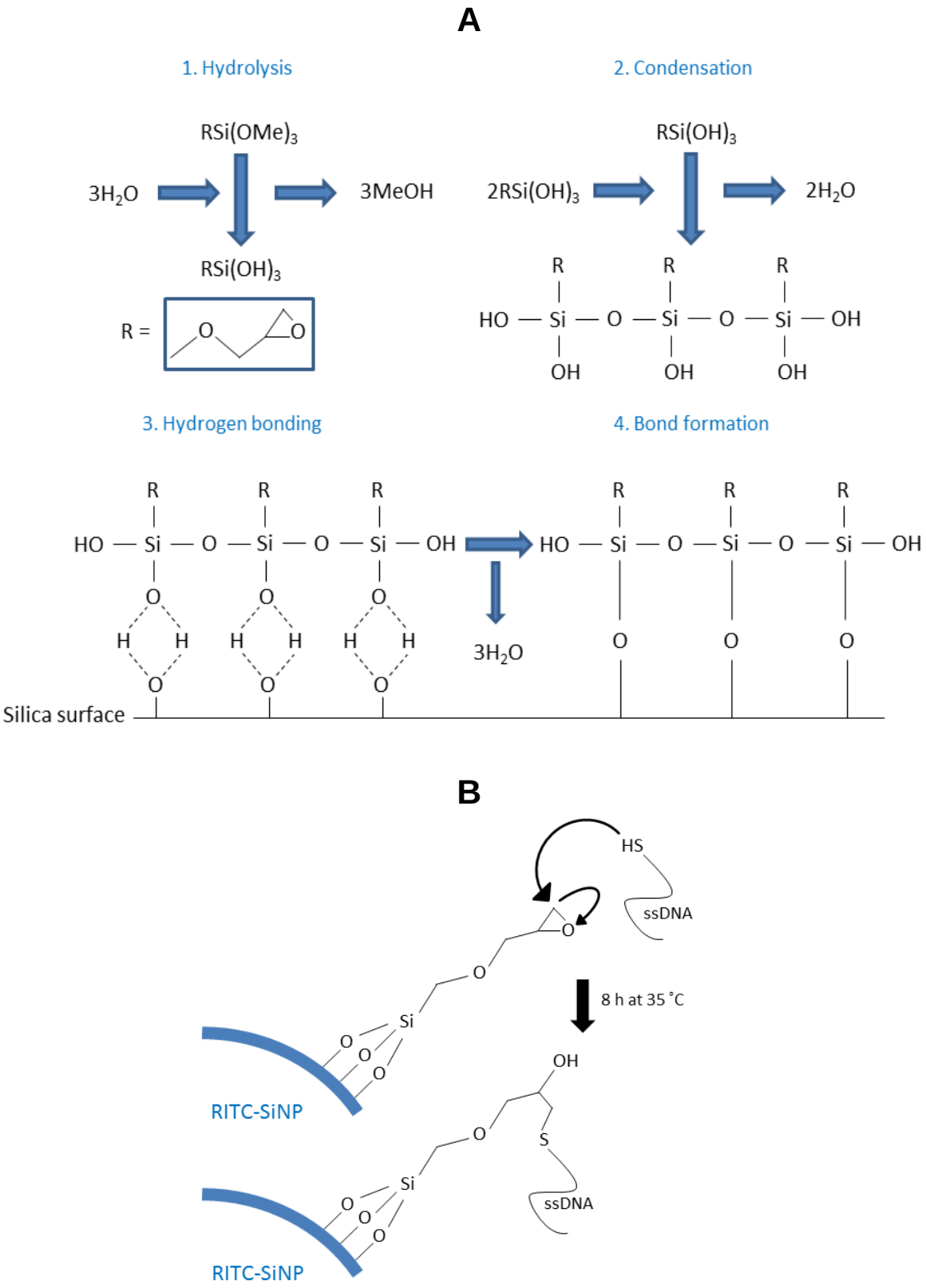

Figure 5 – A - Illustration of the reaction steps involved in the surface functionalization of RITC-SiNPs with GPTMS (the number of covalent bonds formed between the GPTMS and the silica surface is variable); B – thioether linkage between the epoxy group of RITC-SiNP-associated GPTMS and thiolated ssDNA.

Once successfully bound to the surface of the RITC-SiNPs, the GPTMS epoxysilane can act as a linker for the ssDNA probe through a covalent thioether linkage as represented in Figure 5-B [33], while in the case of the gold decorated multifunctional version, the gold nanoclusters provide themselves a platform for binding thiolated oligonucleotides.

5. Gold decoration of dye-doped silica nanoparticles

The gold decoration of dye-doped fluorescent silica nanoparticles aims to combine the fluorescence emission capability of the nanoparticles with the plasmonic-based absorption capabilities of gold nanoparticles, in order to provide the transducer component for a multifunctional DNA biosensor. As discussed in Section 4 in this chapter, the gold decoration also provides a platform for binding thiolated oligonucleotides by covalent bonding [34], therefore dispensing with the need to add a silane linker for binding the ssDNA probe as in the case of the fluorescent-only FL-SiNPs. The gold decoration of silica surfaces has been shown in previous studies by using two methods: the method of two-step seeding of gold nanoparticles on silica [35-37] and the deposition-precipitation (DP) method [38-40] (Figure 6).

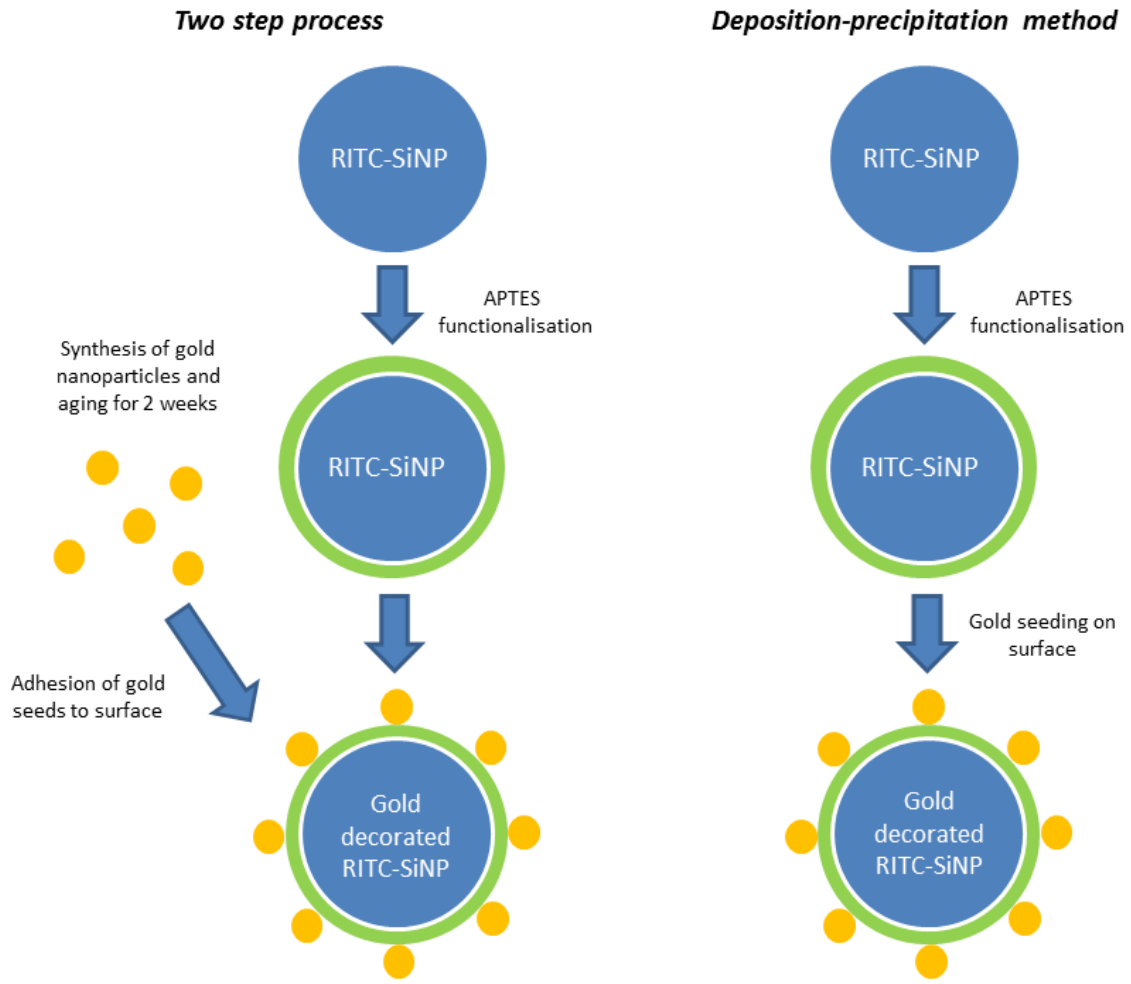

Figure 6 – Main steps in gold decoration of SiNPs by a two-step seeding method and a deposition-precipitation method [40].

The DP method was chosen for the gold decoration of the RITC-SiNPs due to its increased simplicity and effectiveness, given that this method does not require the preparation of gold nanoparticles and two weeks aging prior to seeding on the silica nanoparticles [40]. In general, the DP method consists of placing the silica surface of the RITC-SiNPs in contact with an aqueous solution of gold (III) chloride. The pH of the gold (III) chloride solution is previously raised by the addition of a base in order to increase the proportion of oxidic precursor particles that will act as seeds for the formation of gold nanoclusters on the surface of the RITC-SiNPs. The size and density of the gold nanoclusters can be controlled by changing the concentration of gold (III) chloride as well as the reaction temperature, time and pH. Another important factor is the functionalization of the silica surface prior to DP gold decoration, and previous studies [39] have shown that the effectiveness of gold decoration is significantly reduced on bare silica nanoparticles

due to its low isoelectric point (approximately 2). This implies that the silica surface is negatively charged during the gold seeding due to the high pH necessary for the formation of oxidic precursors, which will hinder the attraction between the precursors and the silica surface. Therefore, the functionalization of the silica surface with a component that presents a sufficiently high isoelectric point is essential for an effective application of the DP process in silica nanoparticles. An approach that has been shown to be successful is the use of 3-aminopropyltriethoxysilane (APTES) to coat the surface of silica nanoparticles in order to raise its isoelectric point [40] [41], and it was one of the approaches that were attempted in this work.

After successful seeding of the gold hydroxide nanoclusters, they can be reduced to gold by adding a reductive agent such as sodium borohydrate [41]. Furthermore, if needed, the resulting gold nanoclusters can be grown by adding gold (III) chloride previously aged in the presence of K_2CO_3, also known as K-gold, to provide additional gold hydroxide that will progressively increase the size of the gold nanoclusters in the silica surface [40] [41]. However, growing the gold decoration may result in reduced light accessibility by the RITC fluorophore inside the silica nanoparticles, and may also result in increased quenching of the fluorophore. One of the greatest technical challenges in building up a combination of fluorescence and plasmonic-based absorption provided by gold nanoclusters in the same nanoparticle is to avoid quenching of the fluorophore. Studies have shown that, in general, gold-fluorophore distances under 5 nm result in strong quenching by the gold [42] [43]. This phenomena is also shown to be correlated with the size of the gold particles in the proximity of the fluorophore (i. e. greater sizes correspond to smaller quenching distance intervals).

In order to avoid quenching of the fluorophore by the gold nanoclusters, the use of one or several layers of the polyelectrolytes polyallylamine hydrochloride (PAH) and polystyrene sulfonate (PSS) [44] [45] as a coating for the RITC-SiNPs was studied in this work. The layer-by-layer approach is achieved by initially coating the negatively charged silica surface of the RITC-SiNPs with the positively charged PAH, followed by subsequent coating with the negatively charged polyelectrolyte PSS until the desired number of layers is obtained (Figure 7). The outermost layer, which will be exposed to the gold seeding should consist of PAH in order to provide an optimum surface charge for the application of the DP method, i. e. neutral or positive charge. Furthermore, building multiple layers should result in the formation of a barrier which will not only support the gold nanoclusters but also create a distance between the RITC encapsulated inside the RITC-SiNPs and the gold decoration, thus potentially reducing quenching of the fluorophore.

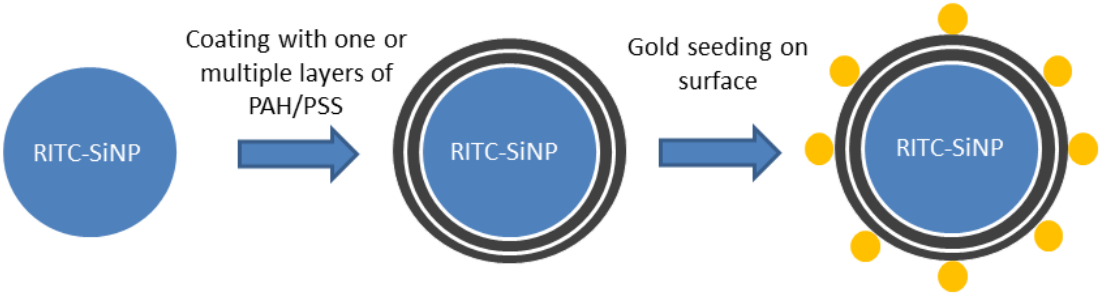

Figure 7 – Schematic for the coating of RITC-SiNPs with a PAH layer or multiple layers of PAH and PSS for gold decoration of RITC-SiNPs.

Chapter II

Materials and Methods

1. Reagents and solvents

Glass materials used throughout the experimental work were thoroughly washed with *aqua regia* (a mixture of nitric acid and chloridric acid in a 1:3 v/v ratio) followed by Milli-Q water, acetone and ethanol (90%), while plastic materials were thoroughly washed with Milli-Q water and ethanol (90%). All aqueous solutions were prepared with Milli-Q water purified at the Analytical Chemistry and Chemistry-Physics Laboratories at the *Departamento de Química e Bioquímica da Faculdade de Ciências da Universidade do Porto* and kindly provided by Prof. Maria João Sottomayor and Prof. António Fernando Silva, respectively.

Synthesis of RITC-doped silica NPs: Rhodamine B isothiocyanate (RITC) 0.1 M aqueous solution was prepared by diluting a mixture of isomers of RITC obtained from Sigma-Aldrich; other reagents used in the synthesis reaction were: ultrapure water obtained from Sigma, Triton X-100 obtained from Sigma-Aldrich, cyclohexane obtained from Sigma-Aldrich, 1-hexanol ($C_6H_{14}O$, 98%) obtained from Merck, tetraethylorthosilicate ($C_8H_{20}O_4Si$, 99.0%) obtained from Aldrich, ammonia solution (25%) obtained from Merck, pure acetone obtained from José M. Vaz Pereira.

Washing cycles by centrifugation: Absolute ethanol obtained from Panreac.

Surface functionalization with GPTMS: Acetonitrile (>99.9%) obtained from Romil, (3-glycidyloxypropyl) trimethoxysilane (>98%) obtained from Aldrich.

Desilylation of GPTMS functionalized RITC-SiNPs: Cesium fluoride obtained from Sigma, deuterated methanol (99.98%) obtained from Sigma-Aldrich.

Surface functionalization with APTES: Absolute ethanol obtained from Panreac, 3-aminopropyltrimethoxysilane (>98%) obtained from Sigma-Aldrich.

Surface coating with PAH/PSS: Polyallylamine hydrochloride (Mw ≈ 15000 and Mw ≈ 56000) obtained from Sigma, polystyrene sulfonate (Mw ≈ 14900) obtained from Polymer Standards Service.

Surface decoration with gold nanoclusters by a deposition-precipitation method: Gold (III) chloride (30% wt in HCl, 99.99%) obtained from Aldrich, sodium borohydrate obtained from Sigma-Aldrich, sodium hydroxide obtained from José M. Vaz Pereira, hydrochloric acid (37%) obtained from Fisher Chemical.

2. Instruments

In order to weigh the compounds used during the experimental work, the analytical scale Mettler AT201 FACT ($2x10^{-5}$ g) was used.

UV-Vis spectrophotometric studies were made using the Varian Cary 50 Bio single beam spectrophotometer with a Starna quartz cuvette (1 cm path length).

Fluorimetry studies were made using the Varian Cary Eclipse fluorescence spectrophotometer with a Starna fluorimetry cuvette (1 cm path length).

Transmission electron microscopy (TEM) images were obtained in a Hitachi H-8100 microscope of the *Departamento de Engenharia dos Materiais do Instituto Superior Técnico* by Dr. Cristina Neves and Dr. Pedro Quaresma, and analysed in the image processing software ImageJ.

Hydrodynamic diameter, polydispersion and zeta potential measurements were obtained in a Zeta Sizer Nano ZS Dynamic Light Scattering (DLS) equipment by Malvern Instruments with a He-Ne 4 mW laser (633 nm).

Fourier Transform Infrared Spectroscopy (FTIR) studies were conducted using the Perkin Elmer Spectrum BX FT-IR system, and the Diffuse Reflectance Infrared Fourier Transform Spectroscopy (DRIFTS) results were obtained using the Jasco FT/IR-460 Plus spectrometer with the diffuse reflectance accessory Easidiff supplied by Pike Technologies.

Atomic force microscopy (AFM) studies were conducted using the AFM Workshop "Long Beach" TT-AFM. All images were obtained with a 50 μm scanner.

^{1}H NMR studies were conducted using the Bruker Avance III 400 NMR spectrometer available at the *Centro de Materiais da Universidade do Porto* operating at 400 MHz.

3. Synthesis of RITC-doped silica nanoparticles

In order to synthesize each batch of rhodamine B isothiocyanate doped silica nanoparticles (RITC-SiNPs), a reverse microemulsion of water (0.340 ml) in cyclohexane (7.50 ml) was prepared in an Erlenmeyer flask using Triton X-100 (1.77 ml) as a surfactant and 1-hexanol (1.80 ml) as a cosurfactant, under agitation. 0.140 ml of 0.1 M RITC solution was added. The mixture became translucid after a few minutes under agitation, and at this point 0.100 ml of ammonia (25%) and 0.060 ml of tetraethyl orthosilicate (TEOS) were added, allowing the formation of silica nanoparticles with the hydrophilic fluorescent dye RITC encapsulated within them (Figure 8).

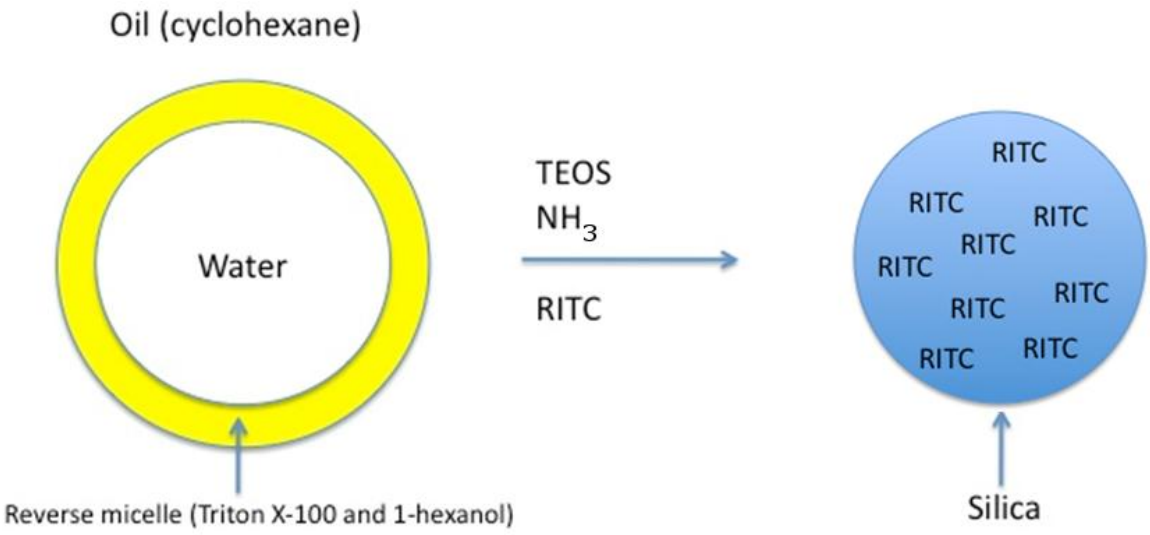

Figure 8 – Schematic representation of the reverse microemulsion synthesis method used for the production of RITC-doped silica nanoparticles.

After 24 hours, 20 ml of acetone were added to the reaction mixture in order to disassemble the micelles around the newly synthesized RITC-SiNPs, and were left without agitation for another 24 hours. The resulting dispersion was subjected to two washing cycles, each one consisting of three centrifugations in absolute ethanol and one in a 1:4 ultrapure water/absolute ethanol mixture. All centrifugations in this step were made at 20,379 g for 20 minutes at 20 ºC. Four batches of RITC-SiNPs were synthesized, named FS-1 to 4, in chronological order (Table 1).

Table 1 – List of synthesized batches of RITC-doped silica NPs and relevant information:

Batches	Amount synthesized (mg)	Relative amount of initial reagents used
FS-1	12.33	1x
FS-2	92.06	4x
FS-3	185.60	8x
FS-4	287.50	12x

4. Functionalization of RITC-SiNPs with GPTMS

The epoxysilane GPTMS was used to allow the binding of thiolated oligonucleotides to the surface of the RITC-doped silica NP batches FS-2 and FS-3. This surface functionalization is based on the covalent bonding between the methoxy groups and the silanol groups at the surface of the RITC-doped silica NPs by a reaction described in Figure 5 (see Section 1.6., Chapter I).

.

To accomplish the aforementioned functionalization, 20 mg of RITC-doped silica NPs were dispersed in 1.25 ml of acetonitrile, and 0.156 ml of GPTMS was added to the dispersion, which was left overnight at 75 ºC under vigorous stirring. The samples were subjected to two washing cycles, each one consisting of three centrifugations in absolute ethanol and one in a 1:4 ultrapure water/absolute ethanol mixture. All centrifugations in this step were made at 20,379 g for 20 minutes at 20 ºC. The batches of GPTMS functionalized RITC-SiNPs obtained are listed in chronological order in Table 2. Different amounts of acetonitrile were tested in order to check for the efficiency of the reaction in a larger amount of solvent, since the redispersion of the FS-2 and FS-3 batches in acetonitrile appeared to be ineffective even after long periods (i.e. 30 minutes) of ultrasonication.

Table 2 – List of batches of RITC-doped silica NPs functionalized with GPTMS, including the amount of acetonitrile used in relation to the protocol described above:

RITC-SiNP batches used	Amount of RITC-SiNPs used (mg)	Batches obtained	Amount obtained (mg)	Relative amount of acetonitrile used
FS-2	20.05	GS-1	10.61	1x
FS-3	50.03	GS-2	32.17	4x
FS-3	49.99	GS-3	34.02	4x
FS-4	20.01	GS-4	12.63	4x

5. Functionalization of RITC-SiNPs with APTES

The aminosilane APTES was used to modify the isoelectric point of the surface of the RITC-SiNPs in order to provide a positive surface charge and thus prevent charge repulsion towards the negatively charged seeding precursors later used in the deposition precipitation process for gold decoration.

To accomplish the aforementioned functionalization, we initially tested the following protocol as a preliminary approach (Experiment 1): 20 mg of plain silica NPs (named PS-1, synthesized under the same protocol as the RITC-doped silica NPs, without the addition of RITC) were dispersed in 4 mL of absolute ethanol to obtain a mass concentration of 5 mg/mL, and 4.69 mL of a 12 mM solution of APTES in absolute ethanol was added to the dispersion and left to react at 80 ºC under vigorous agitation in a round bottom flask for one hour. The sample was subjected to a washing cycle consisting of three centrifugations in absolute ethanol and one in a ultrapure water/absolute ethanol mixture at a 1:4 volume ratio. All centrifugations in this step were made at 20,379 g for 20 minutes at 20 ºC.

A series of experiments were later carried in order to optimize the functionalization. A second approach was made under the same conditions while adding Milli-Q water to the

reaction mixture in a proportion of 75% absolute ethanol/25% Milli-Q water in order to favor the reaction for binding APTES to the surface of the NPs, which follows a mechanism similar to the one described for GPTMS in Figure 5 (see Section 4, Chapter I). Furthermore, we have applied the same protocol with the aforementioned addition of Milli-Q water and without adding any water to the reaction mixture using the RITC-SiNPs batch FS-3. Another modality attempted was to extend the time of reaction without the addition of water to the reaction mixture. This experiment was undertaken by using the batch FS-4, comprising the removal of 100 µL aliquotes at 30 minutes, 1 hour, 3 hours, 4 hours and 24 hours of reaction time. Experiment 5 was carried under the same conditions while changing the amount of APTES to 1/10th of the amount used in Experiment 4. All experiments are listed in Table 3.

Table 3 – List of batches of silica NPs functionalized with APTES:

Experiment	Batch used	Amount of silica NPs used (mg)	Batch obtained	Amount of NPs obtained (mg)
1	PS-1	20.20	AS-1	13.40
2	PS-1	10.00	AS-2	8.02
3	FS-3	10.32	AS-3	9.22
4	FS-4	10.03	AS-4	N/A
5	FS-4	10.00	AS-5	N/A

6. Surface capping of RITC-SiNPs with PAH and PSS

The cationic polymer polyallylamine hydrochloride (PAH) was used as an alternative to APTES as an isoelectric point modifier of the surface of the RITC-SiNPs. The anionic polymer polystyrene sulfonate (PSS) was used in order to build layer-by-layer coatings of PAH/PSS intended to create additional distance between the gold nanoclusters and the RITC encapsulated inside the RITC-SiNPs, thus avoiding quenching

of the fluorophore. Samples were designated by 1L, 3L or 5L according to the total number of polymer layers.

In the case of samples 1L-1 to 1L-3, coating of RITC-SiNPs with PAH was carried by adding PAH solution (200 µL, 10 mg/mL prepared in 10 mM NaCl solution) and NaCl solution (100 µL, 10 mM) to a 1 mg/mL dispersion of RITC-SiNP batch FS-4 in MilliQ water. In all other PAH coatings, PAH solution (200 µL, 10 mg/mL prepared in 10 mM NaCl solution) was added to a 1 mg/mL dispersion of batch FS-4 in 10 mM NaCl solution. PSS coating was carried by adding PSS solution (200 µL, 10 mg/mL prepared in 10 mM NaCl solution) to a 1 mg/mL dispersion in 10 mM NaCl solution of the nanoparticles to be coated. All cappings were carried with the use of PAH of Mw ≈ 15,000 except for 1L-3, which was capped with PAH of Mw ≈ 56,000. After each coating step, all samples were subjected to a washing cycle consisting of three centrifugations in absolute ethanol and one centrifugation in a mixture of ultrapure water and absolute ethanol at a 1:4 volume ratio. All centrifugations in this step were made at 20,379 g for 20 minutes at 20 ºC.

7. Gold decoration of RITC-SiNPs

Gold decoration of RITC-SiNPs was carried by using the following method: 2.25 mL of 0.1 M NaOH solution were added to 7.2 mL of 6.5 mM gold (III) chloride solution in order to obtain a gold hydroxide solution with pH close to 8. 1 mL of APTES functionalized or PAH/PSS coated RITC-SiNPs dispersed in MilliQ water (5 mg/mL) was added to the gold hydroxide solution at 70 ˚C under vigorous stirring and reacted for 30 minutes. The products were washed three times with absolute ethanol and one time with a mixture of MilliQ water and absolute ethanol at a 1:4 volume ratio at 10,000 g for 20 minutes at 20 ˚C. A second set of gold decorations was carried by using $1/10^{th}$ of the gold concentration.

Gold decorated samples were designated by their parent batch designation plus the suffix “–GD”, while the samples subjected to reduction by sodium borohydrate used the suffix “-GDR”.

8. Characterization of the silica nanoparticles

An array of techniques was used to characterize the RITC-doped silica NPs after synthesis and after functionalization with GPTMS, including: UV-Vis spectroscopy, fluorescence spectroscopy, transmission electron microscopy (TEM), size measurements and zeta potential measurements based on dynamic light scattering (DLS), atomic force microscopy (AFM), Fourier transform infrared spectroscopy (FTIR), diffuse reflectance infrared Fourier transform spectroscopy (DRIFTS) and ^{1}H nuclear magnetic resonance spectroscopy (^{1}H NMR).

8.1. UV-Vis spectroscopy

UV-Vis spectroscopy [46] was used to observe the presence of a characteristic absorption band between 550 nm and 570 nm, which corresponds to the absorption of light by the organic dye RITC. Furthermore, this technique was used to monitor the presence of gold in the samples subjected to the DP gold decoration method and to check for the nature of the gold, i. e. bound to the surface or free in solution, including effectiveness of reduction.

All spectra were acquired with 1 mg/ml dispersions of each NP batch in Sigma water.

8.2. Fluorescence spectroscopy

Fluorescence spectroscopy [47] was used to observe the fluorescence of the RITC-SiNPs and their functionalized versions, given that the preservation of RITC fluorescence after encapsulation and surface modifications of the RITC-SiNPs is essential to accomplish the design of the two gene biosensors intended for development, since it provides the transducing functionality to be shared by both biosensors. Furthermore, fluorescence spectroscopy was also used to check for sedimentation of the RITC-SiNPs in aqueous solution.

All spectra were acquired with 1 mg/ml dispersions of each NP batch in MilliQ water, using a 10 nm slit width, a photomultiplier voltage of 650 V, and an excitation wavelength of 549 nm, except in specifically mentioned cases.

8.3. Transmission electron microscopy

Transmission electron microscopy [48] (TEM) is based on the interaction of an electron beam with the sample intended for observation, resulting in the transmission of the beam according to the diffraction of the electrons by the atoms in the sample. The transmitted beam is then magnified, focused, and transformed to a TEM image for further analysis. This technique was used to observe the size, morphology and structural features of the RITC-SiNPs and their functionalized versions, as well as to allow the observation of possible contaminants in the samples.

The samples were prepared by deposition of 10 μL of a 1 mg/ml dispersion of the NPs in MilliQ water in TAAB 200 copper meshes coated with carbon/"formvar".

8.4. Dynamic light scattering

Dynamic light scattering [49] (DLS) is based on the analysis of the Brownian movements of the various particles contained in a given solution or dispersion. A laser beam is used to determine these movements of the particles by measuring the oscillation of light intensity, which in turn allows the determination of the hydrodynamic diameter of the particles by using the Stokes-Einstein equation. The hydrodynamic diameter of a given particle consists of the diameter of a sphere with the same translational diffusion coefficient as the measured particle. This diameter is dependent not only on the size of the particle itself but also on characteristics such as surface charge, solvation, and sample concentration. DLS was used in the present work for determination of the hydrodynamic diameters of the RITC-SiNPs and their functionalized versions.

The measurements were made by using 1 mL of 1 mg/mL dispersions of the NPs in phosphate buffer at a pH of 6.3 and disposable polystyrene DLS size cuvettes (Malvern) at 25.0 ºC, using a thermal equilibrium waiting time of 120 seconds and a

backscattering angle of 173º. Data analysis was made with the Zetasizer software (Malvern).

8.5. Zeta potential measurements

The surface of a particle dispersed in a liquid presents a double layer comprising distinct regions according to their charge. The innermost layer, or Stern layer, presents the surface charge which is related to the ions adsorbed directly in to the object due to various chemical interactions. In turn, the outermost layer, or diffuse layer, is composed of ions attracted to the Stern layer by Coulomb forces. The diffuse layer comprises a specific limit known as sliding plane, inside which the ions move together with the particle. The electric potential in the sliding plane is known as zeta (ζ) potential [50], and can be measured using laser Doppler electrophoresis by applying an electric field to the dispersed particles in a given sample, causing their migration towards the electrode with an opposing charge according to their zeta potential. Therefore, zeta potential measurements are affected by factors such as particle surface composition, temperature, pH and ionic strength. Zeta potential measurements of nanoparticle dispersions were used to measure the colloidal stability of nanoparticles in a given dispersion, since greater absolute zeta potential values correspond to greater repulsions between the nanoparticles, thus indicating lower proneness to aggregation. Zeta potential measurements were also used to monitor changes in surface charge after the various functionalizations applied to RITC-SiNPs, thus providing useful data for measuring success in modifying the surface of the nanoparticles.

1 mg/mL dispersions of the NPs in Sigma water were analysed in disposable polystyrene zeta potential cuvettes with gold-coated electrodes (Malvern) at 25.0 ºC, using a thermal equilibrium waiting time of 120 seconds. Zeta potential measurements were carried with the samples redispersed in phosphate buffer at a pH of 6.3 (unless specifically indicated).

8.6. Atomic force microscopy

Atomic force microscopy [51] (AFM) is a type of scanning probe microscopy that provides high resolution images from a wide variety of samples, as well as nontopographic information by means of other applications such as force spectroscopy (measurement of individual molecular interactions), magnetic force microscopy (measurement of the distribution of the magnetic field of the sample), among others. The imaging capabilities of AFM are provided by scanning a very sharp nanoscale probe along the sample surface. During the scanning procedure, a laser is reflected on the cantilever component of the probe towards a photodetector while the tip component interacts with the sample surface, thus resulting in the measurement of the probe's deflection by the photodetector. This technique allows nanometer resolution scanning due to a combination of various factors such as the reduced size of the probe (ca. 10 nm), sharpness of the tip, high sensitivity of the optical lever and a careful control of forces between the sample and the probe. AFM was used to obtain information about the size and morphology of the RITC-SiNP batches, to provide particle size distribution data for comparison with the TEM and DLS size measurements, and to check for possible contaminations in the RITC-SiNP samples.

AFM images of the synthesized batches of RITC-SiNPs FS-1 and FS-2 were obtained in order to evaluate their size and shape. All images were obtained in "tapping" mode using samples prepared by deposition in mica surfaces of 10 μL of 20x dilutions of 1 mg/mL dispersions of the NPs in Sigma water.

8.7. Fourier transform infrared spectroscopy

Fourier transform infrared spectroscopy [52] (FTIR) allows obtaining an infrared spectrum of a given sample by sequentially shining beams composed by various light frequencies at the sample and measuring the light absorption by the sample at different wavelengths. The FTIR spectra of the fluorophore RITC and the synthesized and functionalized batches of RITC-SiNP batches FS-2 and GS-1 were obtained in order to follow the success of RITC encapsulation inside the NPs and to check for bands characteristic to the GPTMS epoxysilane used to functionalize the surface of the NPs. All measurements were obtained by using KBr disks prepared with 200 mg of KBr and 0.5

mg of each sample. A resolution of 4.0 cm^{-1} was used with a number of 32 scans for each analysis.

Diffuse reflectance infrared Fourier transform spectroscopy [53] (DRIFTS), a modality of FTIR that comprises the measurement of the diffuse reflection produced by shining an infrared light beam onto a given powder sample was used for attempting the detection of the characteristic absorption band of the epoxy group in GPTMS (located at ca. 3050 cm^{-1}) in samples of GPTMS functionalized RITC-SiNPs. The DRIFTS spectra of the functionalized batches of RITC-SiNPs GS-1 and GS-2 were obtained in order to check for bands characteristic to the GPTMS epoxysilane used to functionalize the surface of the NPs. All measurements were obtained by using ground mixtures of 200 mg of KBr and 2.5 mg of each sample. A resolution of 4.0 cm^{-1} was used with a scan number of 256 per analysis.

8.8. ^{1}H nuclear magnetic resonance spectroscopy

Nuclear magnetic resonance (NMR) spectroscopy [54] is a powerful nondestructive technique that allows complete structural and conformational analysis of complex molecules, quantitative analysis of complex mixtures, and noninvasive measurement of reaction rates. NMR spectroscopy is based on the absorption and release of radio frequency (rf) energy by a nucleus in a magnetic field. In order to observe resonance, the nuclei are subjected to electromagnetic radiation with a frequency that matches the precessional frequency of the nuclei. The rf energy is then absorbed by the nuclei in the lower energy spin state, thus raising them to an higher energy spin state, and this energy difference is proportional to the strength of the applied magnetic field. Given that, in the case of bulk matter, nuclei are surrounded by electronic clouds that exert a shielding effect towards the applied field, nuclei with different environments can be identified by using a parameter called chemical shift, which is the resonance frequency measured in relation to that of a reference compound. In the present work, NMR spectroscopy of ^{1}H nuclei was used to evaluate the success of the functionalization of RITC-SiNPs with the silane GPTMS.

The ^{1}H NMR spectra of batch GS-3 was obtained in order to detect the presence of GPTMS after removing it from the surface of the GS-3 nanoparticles by desilylation with 15 mg of cesium fluoride in a 5 mg/mL dispersion of GS-3 for 24 hours in deuterated

methanol [53]. The spectrum of GPTMS was acquired as a control experiment by adding 100 µL of GPTMS to 0.5 mL of deuterated methanol with 15 mg of cesium fluoride. The spectrum of non-desilylated GS-3 NPs was acquired by adding 2.5 mg of GS-3 NPs to 0.5 mL of deuterated methanol. The spectrum of 0.5 mL of the deuterated methanol used in all experiments was also obtained as a control. The NMR spectra were obtained with a 5 mm PABBO BB- probe using deuterated methanol (99.98%) as a solvent. The GPTMS and deuterated methanol spectra were acquired with 32 scans, and the desilylated and non-desilylated GS-3 spectra were acquired with 256 scans.

9. Provenance of functionalized nanoparticle samples

A schematic representation of the provenance of all functionalized nanoparticles synthesized in the present work is shown in Figure 9.

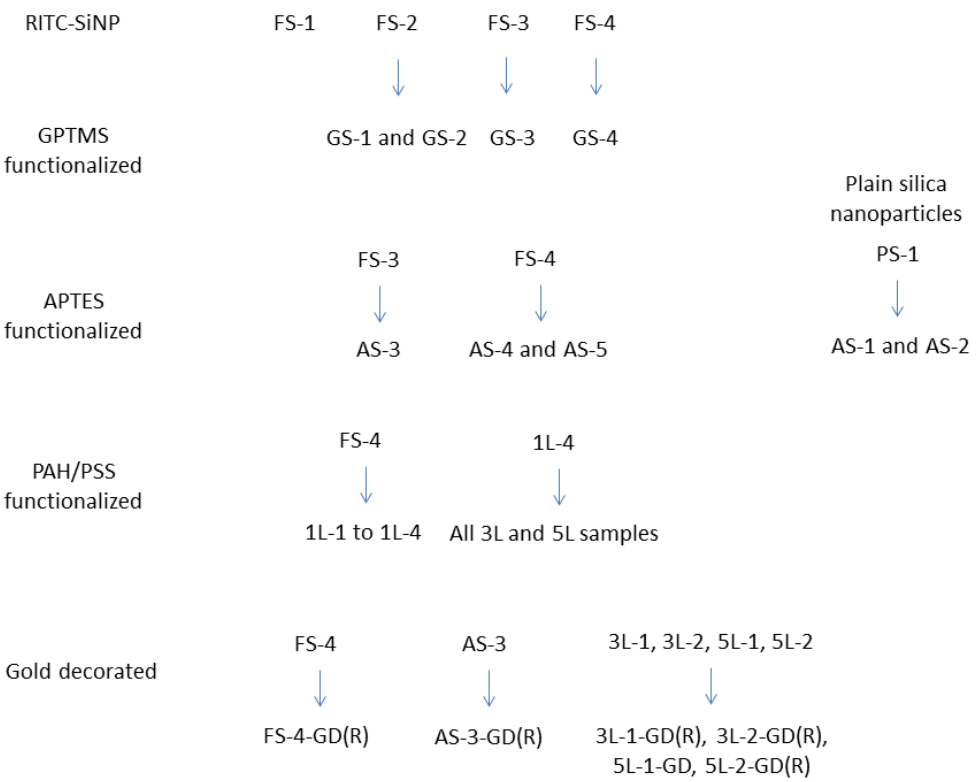

Figure 9 – Schematic overview of functionalized nanoparticles by provenance. Gold decorated samples reduced with sodium borohydrate are labeled with (R).

Chapter III

Results and Discussion

1. RITC-doped silica nanoparticles

1.1. UV-Vis spectroscopy

UV-Vis spectroscopy was used to confirm the presence of RITC encapsulated in the silica NPs by screening for the peak that corresponds to the known excitation wavelength (555 nm) [30] of the RITC fluorophore (Figure 10).

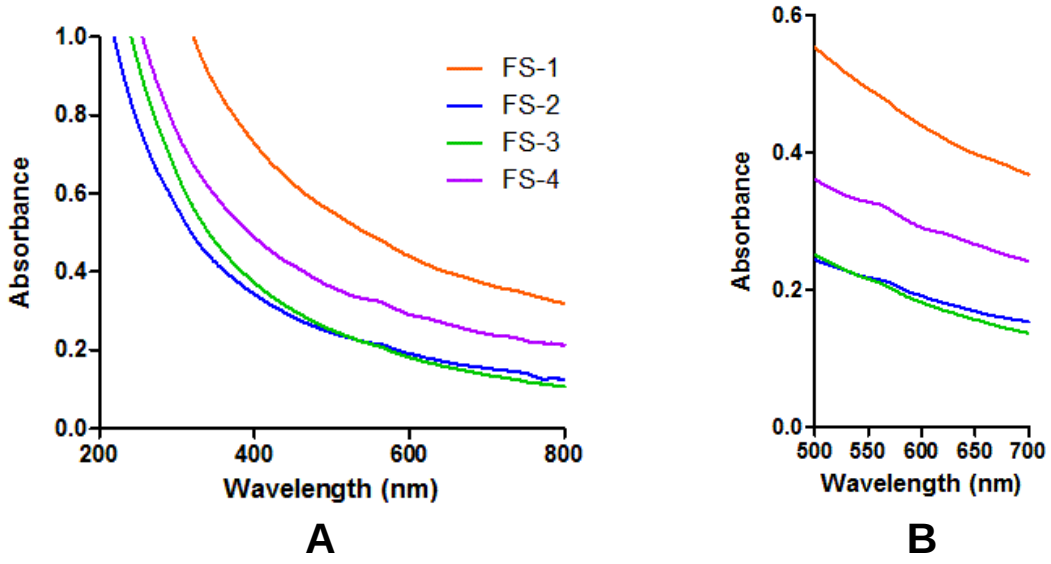

Figure 10 – UV-Vis spectra of each RITC-doped silica nanoparticle (FS) batch (A), including a "zoom-in" of the 550-570 nm region to facilitate visualization (B).

The results for all the RITC silica NP batches (Figure 10) show the presence of a weak peak at ca. 555 nm, indicating the presence of the fluorophore RITC given its characteristic excitation wavelength of 555 nm. However, although the peaks observed in the UV-Vis spectra are consistently present in the same aforementioned region in all samples, they are not very noticeable (Figure 10-B), which is likely due to the prevalence of light scattering by the silica. Therefore, the confirmation of the presence of RITC must be complemented by the use of other techniques such as fluorescence spectroscopy. Furthermore, given that the concentration of NPs in the dispersions used for the measurements is unknown, the absorbance of each curve is expected to show significant differences between the dispersions of each batch. Another possibility is the existence of sedimentation or aggregation of the RITC-SiNPs.

1.2. Fluorescence spectroscopy

The removal of NPs from the dispersion through time was measured for RITC-SiNP batch FS-2 (Figure 11). All fluorescence data was collected while taking into account a well-timed placement and start of each measurement to avoid artifacts related to this variation of fluorescence in time. The obtained data shows a decrease of less than 20% in fluorescence in a period of 60 minutes, pointing towards an ease of sedimentation of the RITC-SiNPs that has been observed by the naked eye during the experimental work.

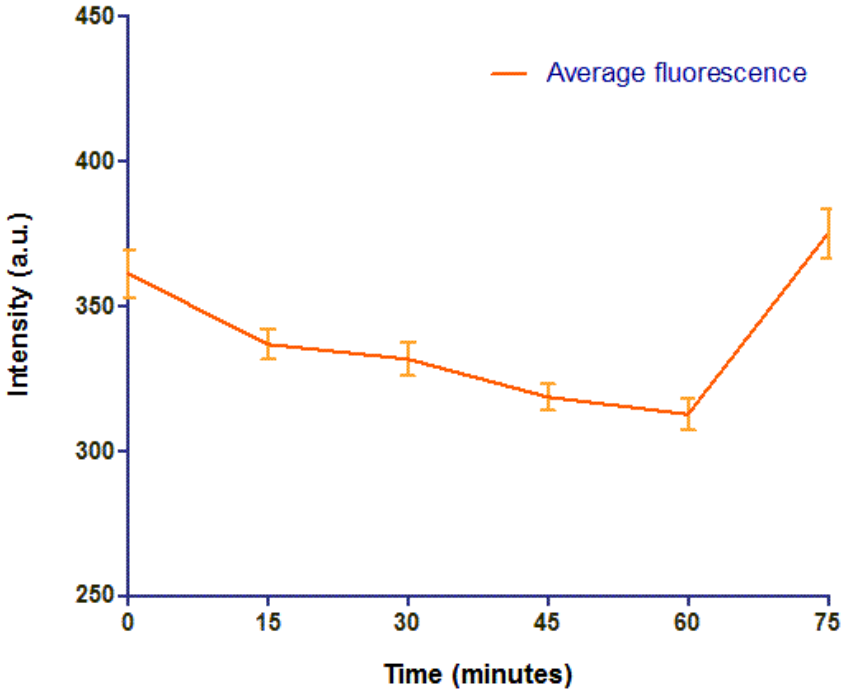

Figure 11 – Fluorescence over time of RITC-SiNP batch FS-2 with redispersion less than 5 minutes before the assay and at 75 minutes of assay time. A 1:15 dilution in Milli-Q water of a 1 mg/mL dispersion of the FS-2 NP batch was used for the measurements.

However, the reduction in fluorescence takes several minutes to become significant. Therefore, all fluorimetry measurements were taken while avoiding significant time lapses between redispersion of the NP samples and analysis.

.

The fluorimetry spectra of each RITC silica NP batch (Figure 12) were acquired in order to check for the existence of RITC encapsulated inside the NPs. As in the UV-Vis spectroscopy results, the peak intensity is variable between each sample, and the cause for this variability is unknown.

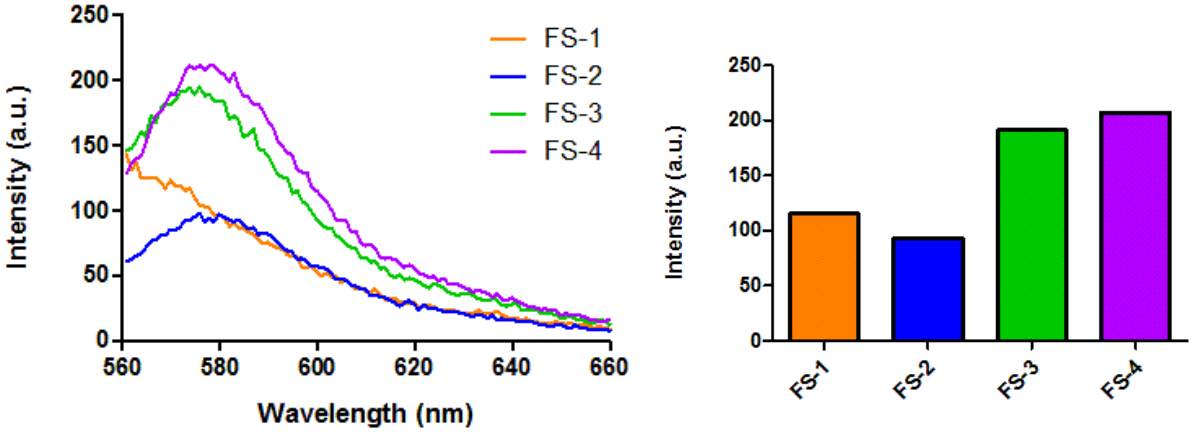

Figure 12 – Fluorescence spectra of each FS batch, including a bar graph representing the fluorescence at a wavelength of 573 nm.

These results indicate the existence of RITC-associated fluorescence in each batch of RITC-SiNPs, which correlates with the UV-Vis results observed for these same NPs, assuming that all RITC not encapsulated inside the NPs was washed away in the centrifugation cycles. The fluorescence at 573 nm of each sample is also represented in Figure 12 for comparison purposes, given that this wavelength is near the maximum emission wavelength of each sample. The fluorescence of sample FS-2 is significantly lower than the fluorescence in samples FS-3 and FS-4, but the cause for this difference is unknown. On the other hand, a correlation between these results and the UV-Vis spectroscopy results does not seem to exist. Sample FS-1 shows a distinct curve in terms of shape and maximum, which could be due to impurities in the sample or to possible differences in the encapsulation of RITC, since it is not known how the RITC distributes itself inside the silica nanoparticles.

1.3. Transmission electron microscopy

The TEM size distribution results for batch FS-1, FS-2 and FS-4 are shown in Figure 13.

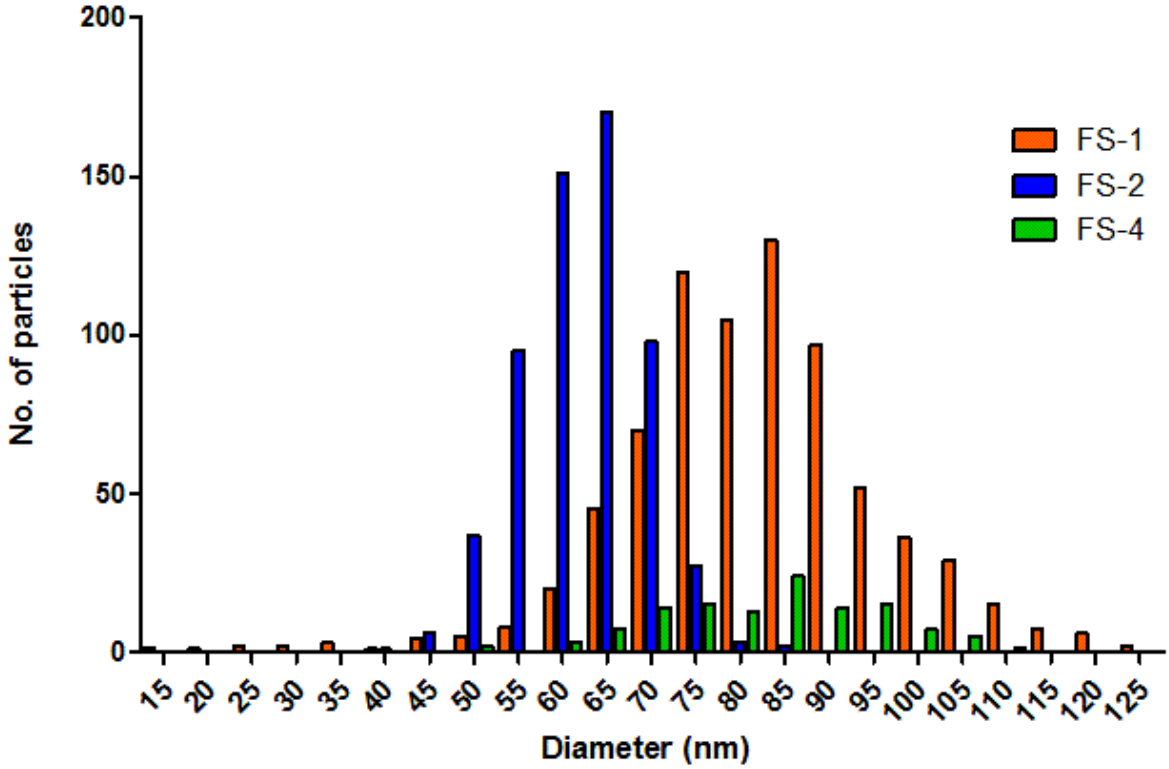

Figure 13 – TEM size distribution results for RITC-doped silica NP batches FS-1 (average diameter: 82 ± 15 nm), FS-2 (average diameter: 63 ± 7 nm) and FS-4 (average diameter: 83 ± 12 nm).

These results show that the synthesis process yields nanoparticles with reasonable size dispersion, given that the standard deviations in all samples are lower than 20% of the corresponding average values. By comparing the three samples analysed, it is possible to observe that the sizes of samples FS-1 and FS-4 are comparable, but sample FS-2 shows an average value approximately 20 nm lower in comparison with the other two samples. The causes for the size dispersion difference in FS-2 are unknown.

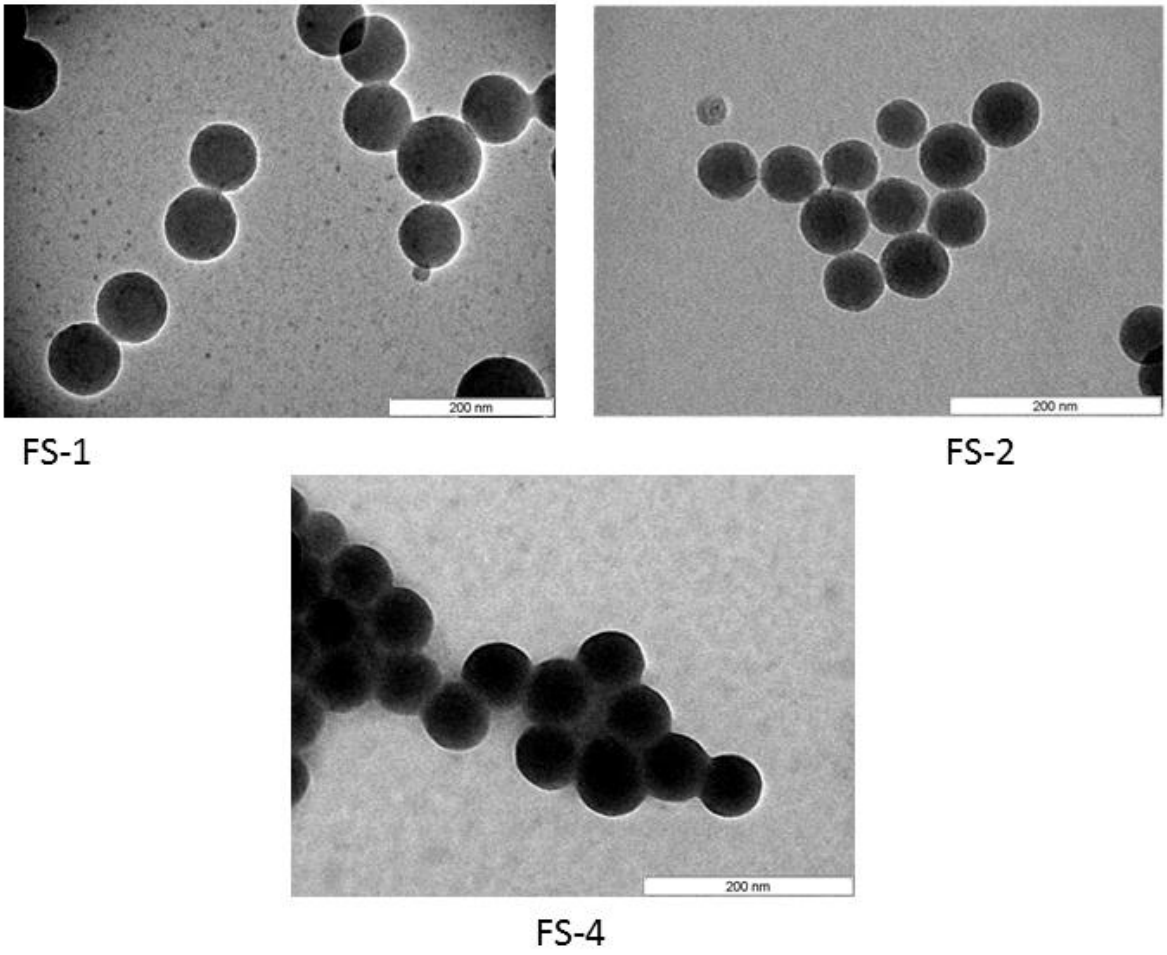

Figure 14 – TEM images of RITC-doped silica NP batches FS-1, FS-2 and FS-4.

TEM images of samples FS-1, FS-2 and FS-4 are shown in Figure 14. It is possible to conclude that the RITC-SiNPs assume a likely spherical configuration given that all particles found in the TEM images show a circular shape. Furthermore, the nanoparticles are well-defined from each other, but show some tendency to agglomerate, which can be interpreted in part as an artifact of their deposition in the TEM grid, and also by a tendency for minimization of exposed surface area.

1.4. Dynamic light scattering

Given that the hydrodynamic diameters account not only for the size of the analysed particles but also for an additional layer that corresponds to the solvent that moves together with the particles on their Brownian movements, it is expected that the average hydrodynamic diameters of the RITC-SiNPs (Table 4) should be larger than the average diameters measured from the TEM results.

Table 4 – Average hydrodynamic diameter of the synthesized RITC-SiNP batches:

Batches	FS-1	FS-2	FS-3	FS-4
Average hydrodynamic diameter (nm)	100±2	70±6	67±5	70±16

The results shown in Table 4 indicate a narrow size dispersion between the FS samples. It can also be concluded that particle agglomeration is not significant after the redispersion by sonication for 5 minutes applied to each sample before the DLS measurements, which were carried a few minutes after, although it was observable that a period of a few hours is enough to visualize with the naked eye the sedimentation of the RITC-SiNPs. The narrow size dispersion of the FS batches is also observable in Figure 15.

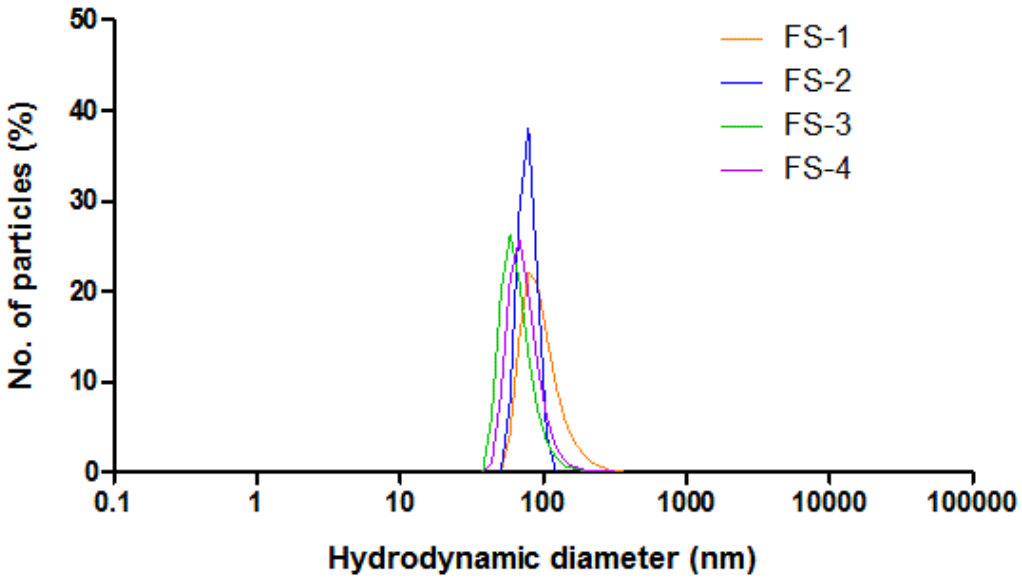

Figure 15 – DLS hydrodynamic diameter distribution (by percentage of number of particles) for RITC-doped silica NP batches FS-1, FS-2 and FS-4.

1.5. Zeta potential measurements

The results for the zeta potential measurements of the RITC-SiNP batches (Table 5) are very consistent between samples, thus pointing to a good reproducibility in terms of surface charge. This consistency is in agreement with the expected composition of the surface RITC-SiNPs, which is the exposure of silanol groups that confer a negative charge to the surface, thus providing a good indicator for the adequacy of the RITC-SiNPs for the surface modifications studied in this work.

Table 5 – Zeta potential of RITC-doped silica NPs:

Batches	FS-1	FS-2	FS-3	FS-4
Zeta potential (mV)	-29.6±1.2	-29.7±0.8	-29.8±0.9	-29.7±1.4

1.6. Atomic force microscopy

The AFM images of the RITC-doped silica NP batches FS-1 and FS-2 are shown in Figure 16. The structures shown in the images are likely individual silica nanoparticles and their agglomerates, given that the sizes of the smaller and individualized units have been found to be in agreement with the dimensions given by the TEM size measurements (Table 6), although it should be noted that the number of particles available for measurement in the AFM images is much smaller than in the case of TEM measurements. The AFM data are also consistent with the likely spherical shape of the RITC-SiNPs observed in the TEM images.

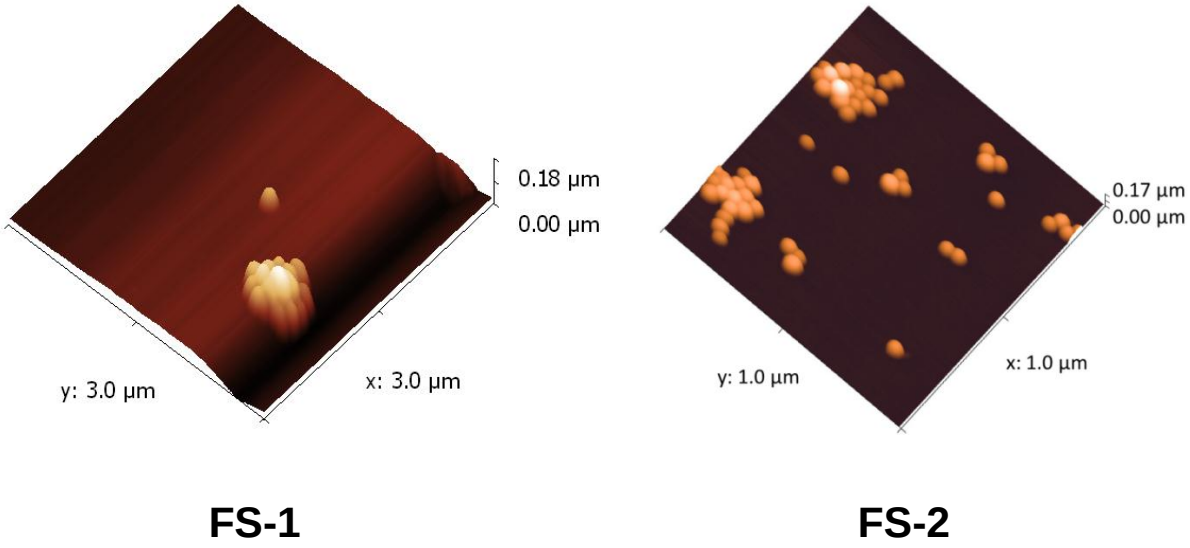

Figure 16 – AFM images of the RITC-doped silica NP batches FS-1 and FS-2.

Table 6 – Average diameter measured by AFM of the RITC-SiNP batches FS-1 and FS-2, including comparison with TEM results and number of particles analysed in each method:

Batches	FS-1	FS-2
AFM average diameter (nm)	75±13	71±17
Number of particles analysed	13	67
TEM average diameter (nm)	82±15	63±7
Number of particles analysed	1028	697

2. Functionalization of RITC-SiNPs with GPTMS

2.1. Fluorescence spectroscopy

The fluorimetry spectra of each GS batch (Figure 17) were acquired in order to check for the existence of RITC encapsulated inside the NPs.

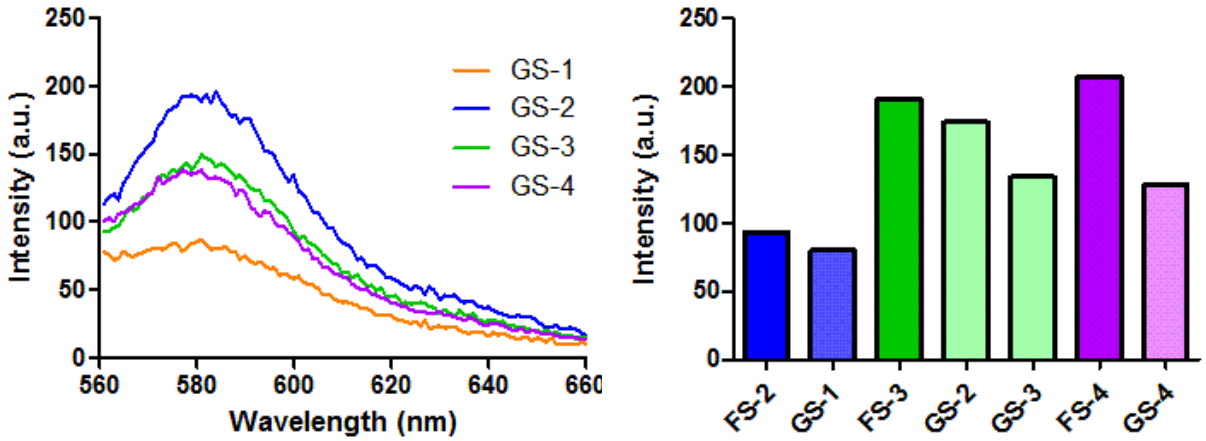

Figure 17 – Fluorescence spectra of each GS batch, including a bar graph representing the fluorescence at a wavelength of 573 nm of each GS batch and of the respective original FS samples for comparison purposes.

The results indicate the existence of RITC-associated fluorescence in each GS batch, but the GPTMS functionalization appears to have affected significantly the fluorescence of the FS parent batches used in the case of samples GS-3 and GS-4. However, it is not possible to draw a reliable conclusion whether the fluorescence decrease was due to loss of RITC during the functionalization or due to other possibilities such as an increase of particle weight that would reduce the amount of RITC per mass of NPs, given that the dispersions used for the fluorescence assays have the same mass concentration and an unknown NP concentration. Nonetheless, the fluorescence of the RITC-SiNP samples is not affected in a severe way after GPTMS modification.

2.2. Transmission electron microscopy

The TEM size distribution results for batch GS-3 are shown in Figure 18. Comparison of the GS-3 TEM average size with a TEM average size of the parent batch FS-3 is not possible given that no TEM images of the latter were acquired. Comparison of Figure 18 with Figure 12 allows us to observe that the size dispersion of GS-3 is comparable to the dispersion shown by the FS samples.

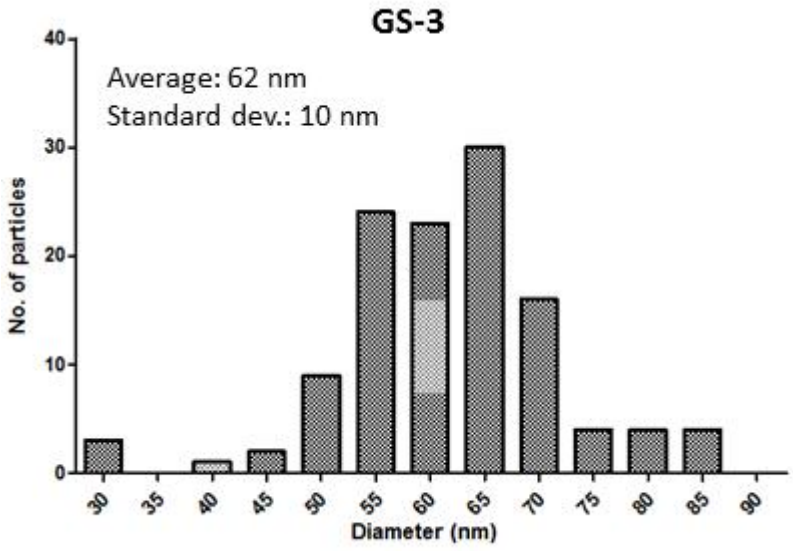

Figure 18 – TEM size distribution results for batch GS-3.

A TEM image of the GS-3 sample is shown in Figure 19. It is observed that the NPs are similar in shape and size to the RITC-SiNPs, which is expected given that an existing monolayer of GPTMS would not be visible by TEM due to its small size.

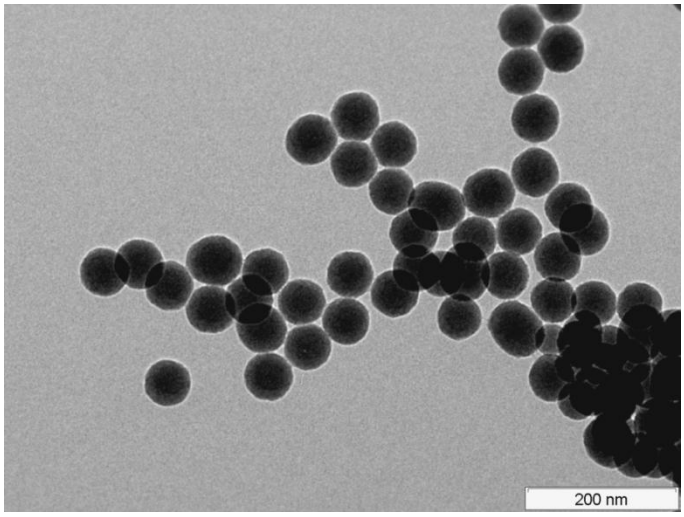

Figure 19 – TEM image of GPTMS functionalized RITC-SiNPs GS-3.

2.3. Dynamic light scattering

The DLS size measurement results are shown in Table 7. Samples GS-2 to 4 show average hydrodynamic diameters significantly higher in comparison with their non-functionalized parent batches; in turn, the GS-1 sample did not show such an increase in hydrodynamic diameter.

Table 7 – Average hydrodynamic diameter of GPTMS functionalized RITC-SiNP batches, including comparison with their respective parent batches:

Batches	GS-1	GS-2	GS-3	GS-4
Average hydrodynamic diameter (nm)	68 ± 3.0	106 ± 8.4	109 ± 2.2	141 ± 20.5
Parent batch average hydrodynamic diameter (nm)	70 ± 5.9	67 ± 5.0	67 ± 5.0	70 ± 15.7

Figure 20 shows the hydrodynamic diameter distributions for the GS samples. It is observable in Figure 20 that the size dispersion of the GS nanoparticles is narrow, as in the case of the original FS batches (Figure 14).

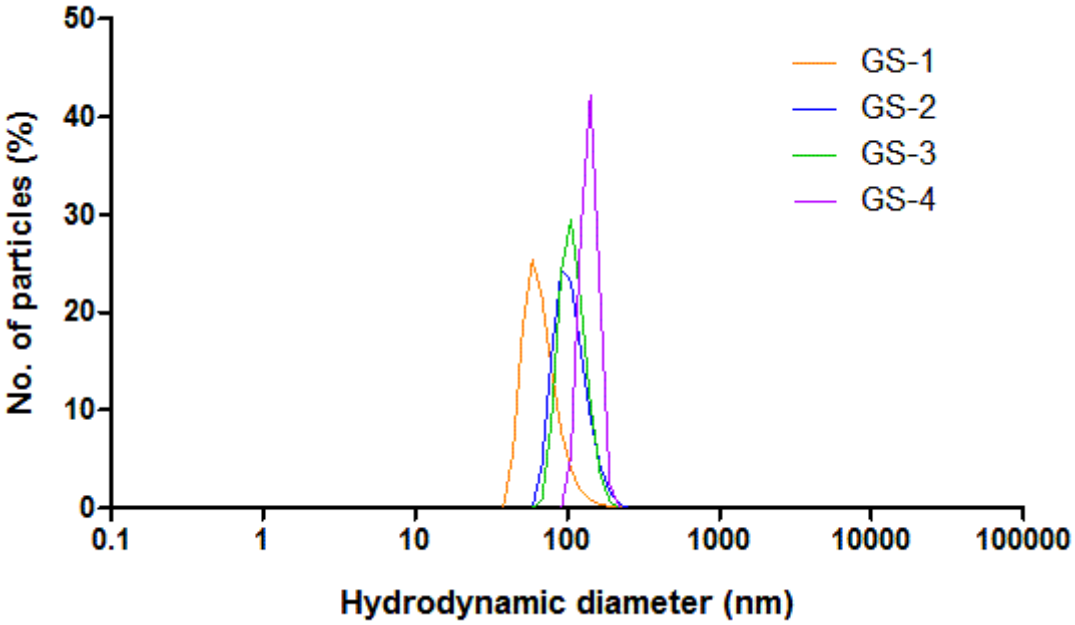

Figure 20 – DLS hydrodynamic diameter distribution (by percentage of number of particles) for GPTMS modified silica NP batches GS-1, GS-2, GS-3 and GS-4.

2.4. Zeta potential measurements

The results for the zeta potential measurements of the RITC-SiNP batches are shown in Table 8. Samples GS-2 to 4 all show a decrease in absolute value which is very consistent, while sample GS-1 does not show any significant change in zeta potential in comparison with its parent batch. These results support the hypothesis that samples GS-2 to 4 were all successfully functionalized with GPTMS while sample GS-1 was not effectively functionalized.

Table 8 – Average zeta potential of GPTMS functionalized RITC-SiNP batches:

Batches	GS-1	GS-2	GS-3	GS-4
Zeta potential (mV)	-30.3 ± 1.4	-22.9 ± 1.4	-22.4 ± 1.6	-22.6 ± 0.6
Zeta potential of parent batches (mV)	-29.7 ± 0.8	-29.8 ± 0.9	-29.8 ± 0.9	-29.7 ± 1.4

The GPTMS functionalizations that provided samples GS-2 to 4 did use a proportion of four times more acetonitrile for redispersion of the RITC-SiNPs in comparison with GS-1, which might have a relevant influence on the reaction effectiveness due to differences in NP redispersion. Therefore, the use of four times less acetonitrile might have prevented the GPTMS functionalization due to the inaccessibility of GPTMS to the surface of the NPs. The redispersion of the RITC-SiNPs in four times less acetonitrile has shown to be ineffective by naked eye observation of the nanoparticle sample, whereas in the case of the redispersions with four times more acetonitrile the amount of non-dispersed nanoparticles was clearly reduced.

2.5. Fourier transform infrared spectroscopy

The FTIR spectrum of the fluorophore RITC is shown in Figure 21, and the spectra of the FS-2 RITC-SiNP batch and GS-2 GPTMS functionalized batch are shown in Figure 22.

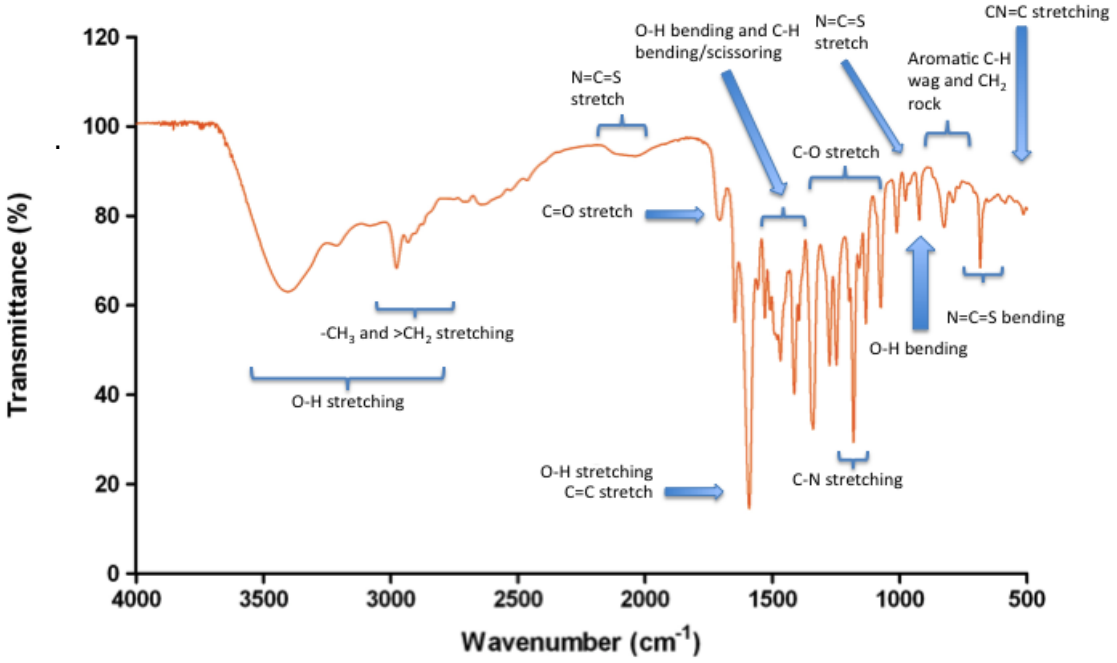

Figure 21 – FTIR spectrum of rhodamine B isothiocyanate (assignments based on correlation charts at www.vidrine.com).

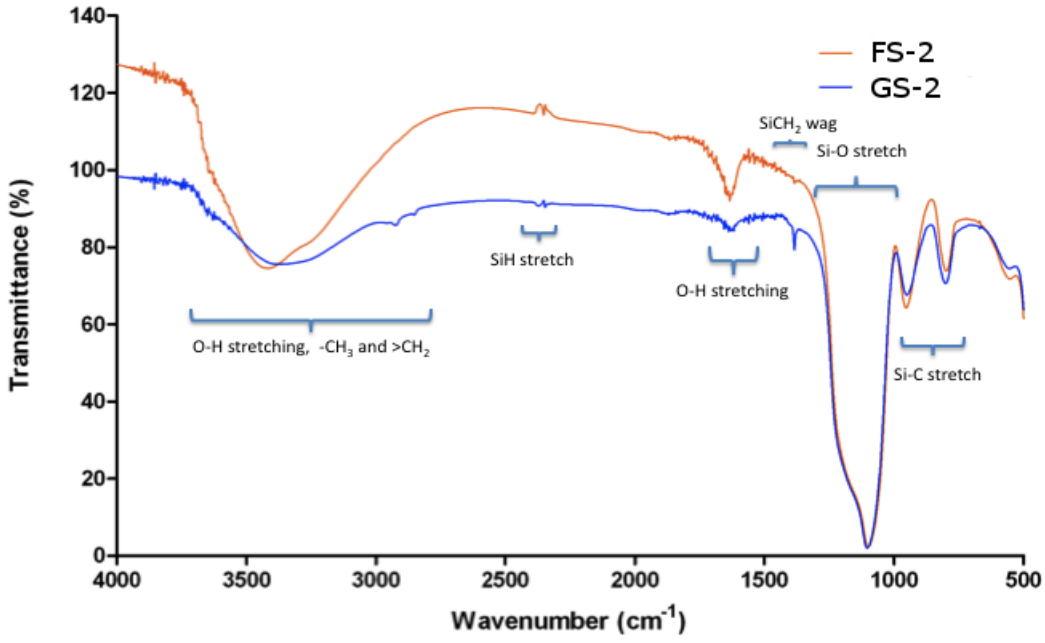

Figure 22 – FTIR spectra of the RITC-SiNP batch FS-2 and GPTMS functionalized batch GS-2 (assignments based on correlation charts at www.vidrine.com).

The bands found in the FTIR spectrum of RITC (Figure 21) are in agreement with the expected results, given the large variety of vibrational modes that can be found due to the chemical structure of the fluorophore (Figure 23).

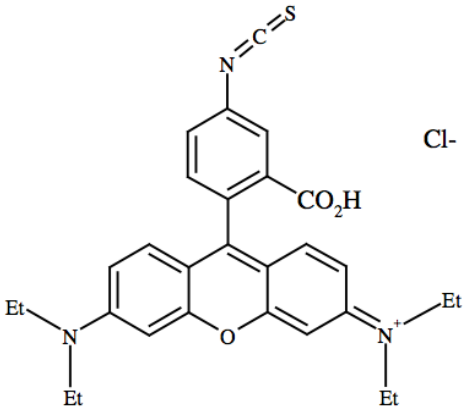

Figure 23 – Chemical structure of rhodamine B isothiocyanate.

By comparing the spectra of the FS-2 and GS-2 batches (Figure 22), it is possible to observe that the bands characteristic of the silica structure are prevalent in both cases, and that the characteristic band at 3050 cm^{-1} indicating the presence of the epoxy group of the silane GPTMS is not visible. This does not imply necessarily the absence of GPTMS at the surface of GS-2 NPs, given that the characterictic band for the epoxy could be masked by the other prevalent band in the same region. Another possible explanation for the absence of the 3050 cm^{-1} band is the possibility of opening of the epoxy ring by hydrolysis; however, this is unlikely because it would require the presence of an acid catalyst to occur in a wide scale.

2.6. Diffuse reflectance infrared Fourier transform spectroscopy

The DRIFTS spectra of GPTMS functionalized samples GS-2 and GS-3 (Figure 24) were obtained in order to attempt the detection of the epoxysilane GPTMS through visualization of the characteristic epoxide band at 3050 cm^{-1}, given that this band was undetectable by FTIR (Section 2.6).

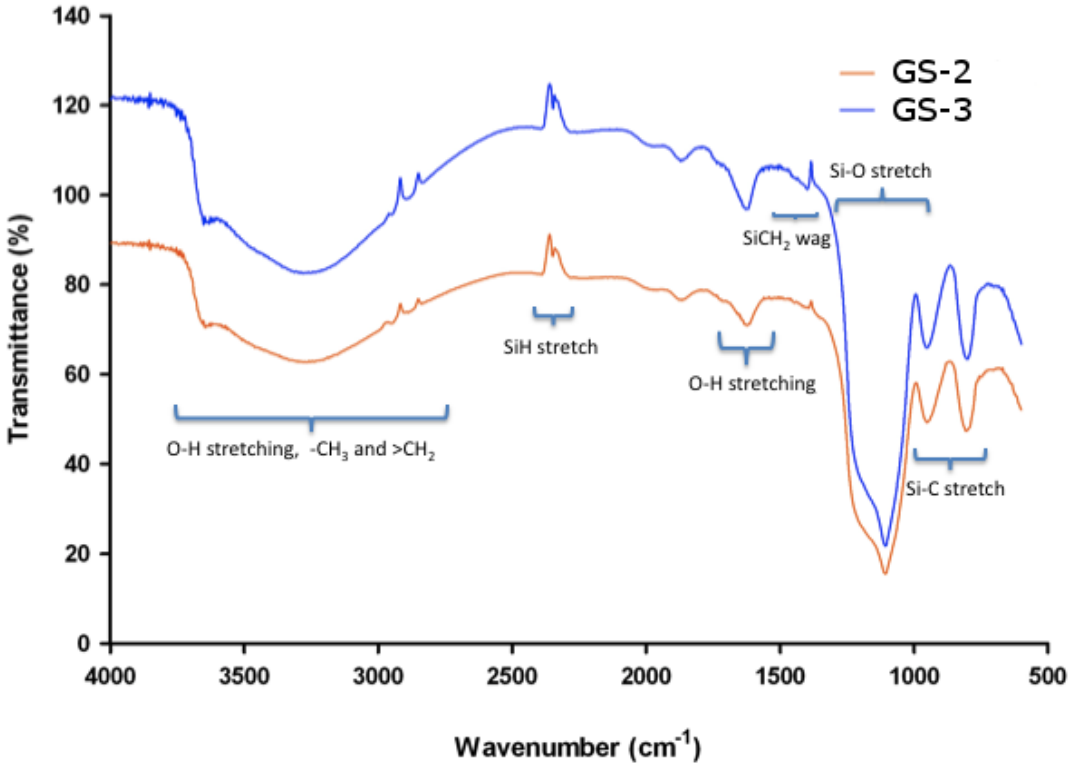

Figure 24 – DRIFTS spectra of the GPTMS functionalized batches GS-2 and GS-3 (assignments based on correlation charts at www.vidrine.com).

As in the FTIR spectrum of GS-2, the DRIFTS spectra of GPTMS functionalized samples GS-2 and GS-3 (Figure 24) do not show the characteristic band for the epoxy group of GPTMS, and the possible causes for this are the ones discussed in Section 2.6. This has prompted the attempt of using NMR to detect the presence of GPTMS in the GPTMS functionalized sample GS-3, which will be discussed in the following section.

2.7. ^{1}H nuclear magnetic resonance spectroscopy

^{1}H NMR spectroscopy of the GPTMS functionalized sample GS-3 was carried out in order to detect the GPTMS epoxysilane through the characteristic environments surrounding the hydrogen nuclei in the GPTMS molecule. Furthermore, this technique was also used for obtaining information related to the chemical environment of the hydrogen nuclei that are present in the epoxy group of GPTMS, allowing us to verify the possibility of hydrolysis of the epoxy group to a glycol. However, this detection required the previous desilylation of GPTMS from the surface of the NPs, given that the attachment of GPTMS to the surface of the much larger GS-3 NPs would prevent the detection of the epoxysilane due to transverse relaxation related to the large size of the GPTMS-NP complex, since the tumbling rate of the complex is very low in comparison with the tumbling rate of free GPTMS [55] [56].

The ^{1}H NMR spectrum of sample GS-3 after desilylation with cesium fluoride [53] (Figure 25-A) was thus acquired for the detection of GPTMS, The spectrum of the GPTMS used in all functionalizations attempted (Figure 25-B) was acquired for comparison. The spectrum of GS-3 without desilylation (Figure 26) was acquired as a control experiment, and the spectrum of the deuterated methanol (Figure 27) used as a solvent in all NMR experiments was also obtained in order to check for the existence of solvent and impurities. The ^{1}H NMR spectrum of sample GS-3 in Figure 25-A shows that the desilylation with cesium fluoride has resulted in the removal of GPTMS from the NP surface, thus enabling the detection of the epoxysilane by NMR. In turn, the spectrum of GPTMS (Figure 25-B) allows confirmation of the presence of GPTMS in the desilylated GS-3 sample. The spectrum obtained from non-desilylated GS-3 (Figure 26) does not show any peak specific to GPTMS H nuclei, which indicates that the GPTMS epoxysilane is stably interacting with the surface of the nanoparticles, which is in agreement with the occurrence of covalent bonding between the silanol groups presented by the silica surface and the trimethoxy moiety of GPTMS. Furthermore, the absence of peaks specific to GPTMS H nuclei in the spectrum of non-desilylated GS-3 is in agreement with the expected low tumbling rate of GPTMS bound to the surface.

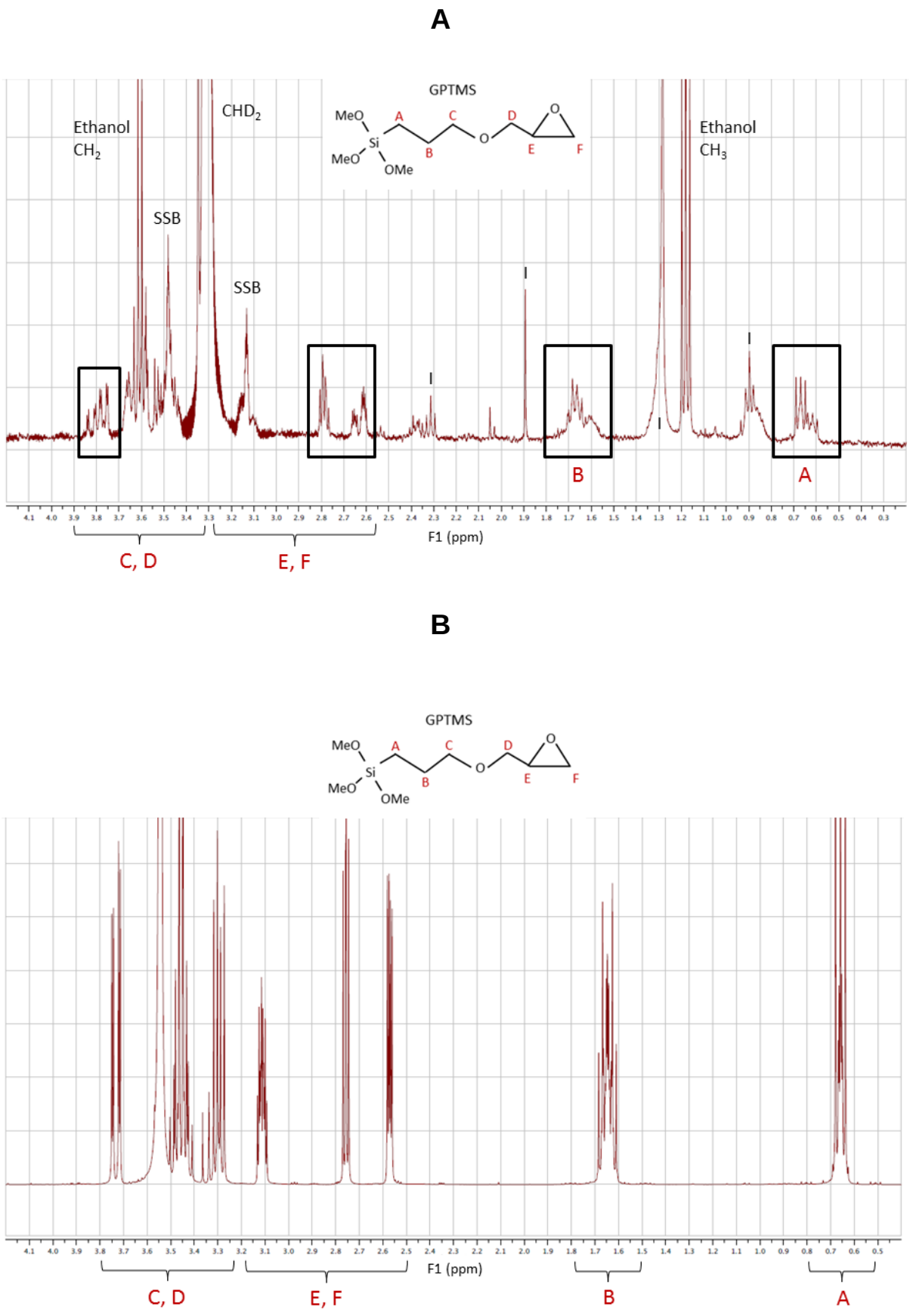

Figure 25 – A - ^{1}H NMR spectrum of the GPTMS functionalized batch GS-3 after desilylation (SSB – satellite band; I – impurity), including assignments of GPTMS H nuclei; B - ^{1}H NMR spectrum of the GPTMS epoxysilane, including assignments of GPTMS H nuclei (SSB – satellite band; I – impurity).

It is also observable by comparing Figures 25, 26 and 27 that all unidentified impurities found in the desilylated and non desilylated GS-3 samples are likely the same impurities provenient from the deuterated methanol; however, these impurities were not found in the GPTMS spectrum. Given that the GPTMS spectrum was the first one to be obtained in chronological order, it is likely that the impurities were introduced in the deuterated methanol after acquiring the GPTMS spectrum.

The spectrum of desilylated GS-3 shows two peaks specific for ethanol, and this presence may be due to the use of ethanol in the washing procedure of the NPs that may have remained in the sample. Removal of ethanol was attempted by vacuum drying, but the spectrum obtained after the procedure was similar to the spectrum in Figure 25-A, therefore it is not shown in this work. However, future attempts to remove the ethanol would be relevant due to the covering of GPTMS specific peaks by the ethanol peak corresponding to the CH_2 H nuclei. Furthermore, the splitting of the peak corresponding to the H nuclei designated by F in Figure 25-A is not known as to its cause, and further work should be carried to obtain such information.

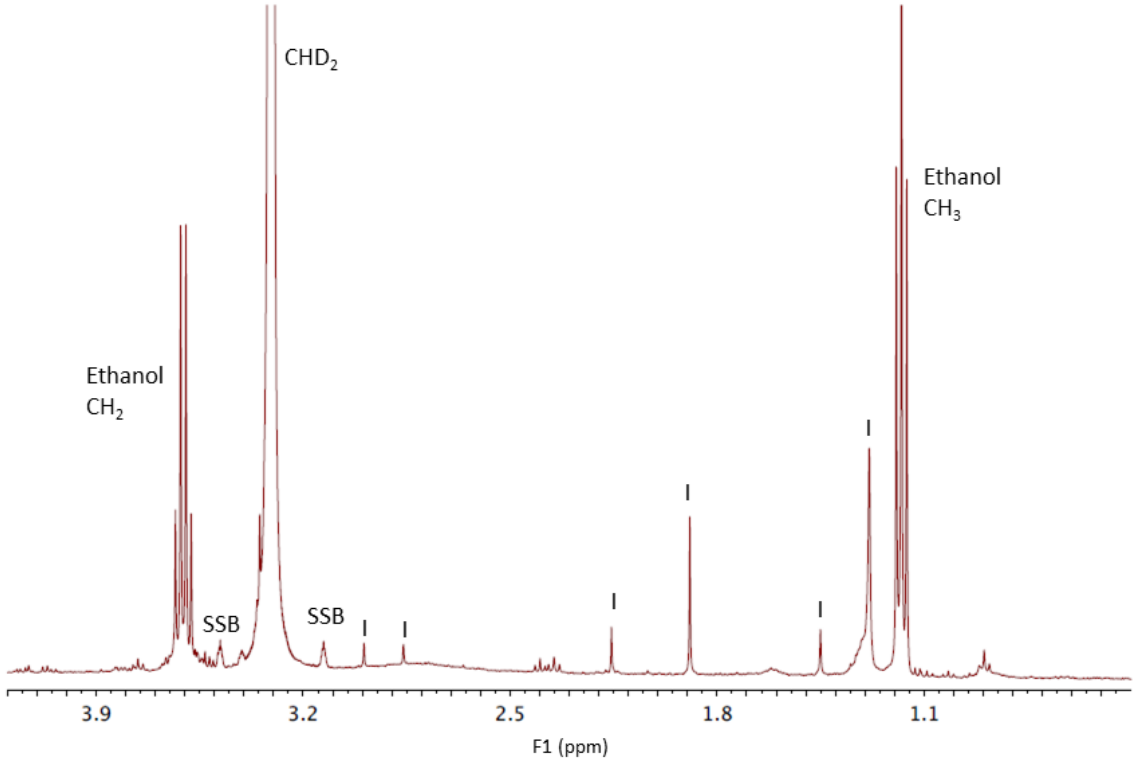

Figure 26 – ^{1}H NMR spectrum of the GPTMS functionalized batch GS-3 without desilylation by cesium fluoride (SSB – satellite band; I – impurity).

The hypothesis that the epoxy group would be hydrolyzed into a glycol was studied by using the NMR results in Figure 25-A. If the epoxide had been hydrolyzed, a significant upfield shift of the peak coupled with a reduction in relative peak intensity would be expected; however, when comparing the peaks in Figure 25-A with the GPTMS peaks in Figure 25-B it is observable that their respective chemical shifts do not show significant differences, thus indicating that the epoxy ring is stable under the storage and experimental conditions to which the sample was subjected.

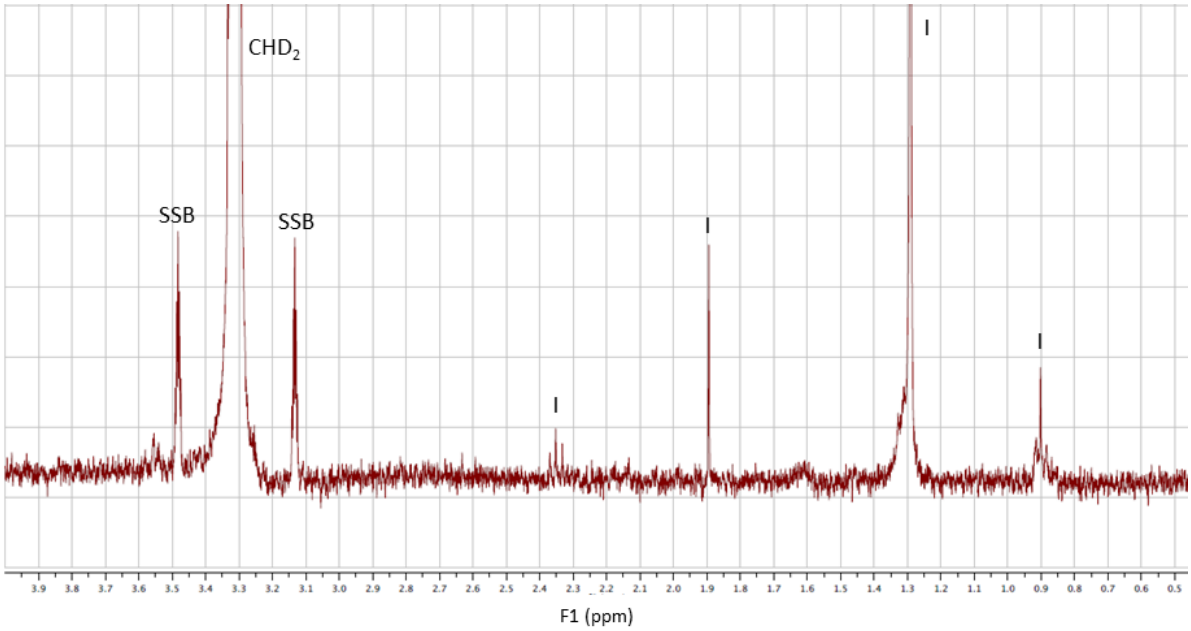

Figure 27 – ^{1}H NMR spectrum of the deuterated methanol used in all NMR experiments (SSB – satellite band; I – impurity).

These results allow us to conclude that the GPTMS functionalization was successful for sample GS-3. Furthermore, they also allow us to conclude that the GPTMS is bound to the surface by a strong interaction, most likely covalent bonding to the silanol groups on the surface of the NPs, given that the non-desilylated GS-3 sample did not show any peaks specific to the presence of GPTMS.

3. Functionalization of RITC-SiNPs with APTES

3.1. Fluorescence spectroscopy

The fluorimetry spectra of APTES functionalized samples AS-1 and AS-3 are shown in Figure 28 as representative of the fluorescence observed in all APTES functionalized samples. The spectra of the remaining APTES functionalized samples are omitted for visualization purposes, given that all APTES functionalized samples show similar fluorescence curves.

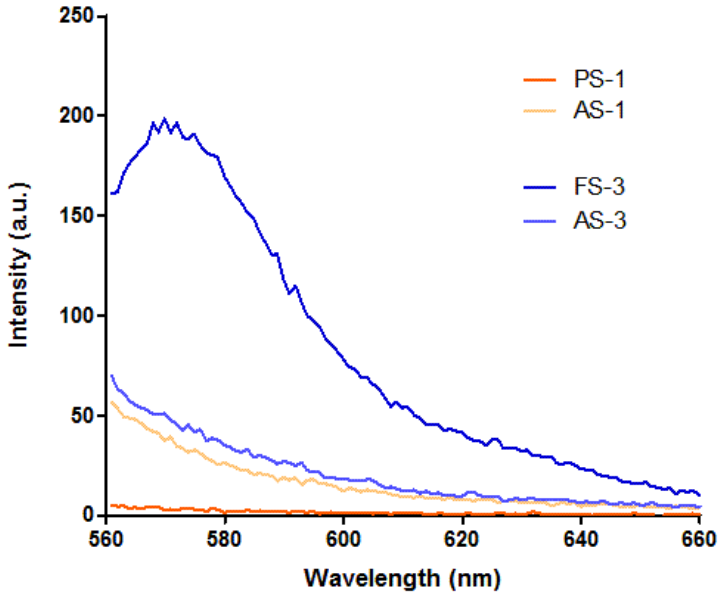

Figure 28 – Fluorescence spectra of APTES functionalized batches AS-1 and AS-3, including the spectra of their corresponding parent batches PS-1 and FS-3.

The fact that all APTES functionalized samples show similar curves indicates that the fluorescence curves are likely due to scattering by the presence of APTES, and that the fluorophore RITC does not contribute to it. This interpretation is strengthened by observing that the AS-1 sample shows a curve similar to the AS-3 sample, although AS-1 is a modification of the plain silica NP sample PS-1 and AS-3 comes from the RITC-SiNP sample FS-3. This indicates that the functionalization with APTES affects significantly the fluorescence capability of the NPs, probably due to the formation of self-polymerized APTES during the functionalization reaction. Furthermore, although sample AS-3 shows

the absorbance peak specific for the RITC fluorophore in the UV-Vis spectroscopy results, the fluorescence emission that is expected to result from this absorbance is likely to be scattered by the self-polymerized APTES. This has been further studied by using DLS size measurements to evaluate the formation of self-polymerized APTES, which will be discussed in the following section.

3.2. Dynamic Light Scattering

The DLS size measurement results in Table 9 show that the average hydrodynamic diameter of all APTES functionalized samples is, in general, significantly higher in comparison with the values for the corresponding parent batches. This indicates the consistent formation of self-polymerized APTES in every sample.

Table 9 – Average hydrodynamic diameter of APTES functionalized batches (AS) (Experiments 1, 4 and 5 follow the original protocol without addition of water; 2 and 3 include the addition of water at a 1:3 v/v ratio, 5 uses 1/10th of original APTES amount):

Experiment	Parent batch	Average hydrodynamic diameter (nm)	Batch obtained	Reaction time (hours)	Average hydrodynamic diameter (nm)
1	PS-1	69 ± 1.4	AS-1	1	106 ± 12
2	PS-1	69 ± 1.4	AS-2	1	437 ± 53
3	FS-3	67 ± 5	AS-3	1	733 ± 210
4	FS-4	70 ± 16	AS-4	0.5	1182 ± 70
4	FS-4	70 ± 16	AS-4	1	710 ± 460
4	FS-4	70 ± 16	AS-4	3	1517 ± 711
4	FS-4	70 ± 16	AS-4	4	3207 ± 2252
4	FS-4	70 ± 16	AS-4	24	249 ± 160
5	FS-4	70 ± 16	AS-5	0.5	3551 ± 1084
5	FS-4	70 ± 16	AS-5	1	1861 ± 480
5	FS-4	70 ± 16	AS-5	3	1541 ± 1497
5	FS-4	70 ± 16	AS-5	4	75 ± 24
5	FS-4	70 ± 16	AS-5	24	202 ± 169

All AS samples show either high hydrodynamic average diameters or high standard deviations between measurements in comparison with their parent batches. In turn, the hydrodynamic diameter distributions in Figure 29 show the presence of large particles in the majority of the samples. The self-polymerization of APTES in solution is known to be due to the condensation of the three ethoxy groups present in APTES with the ethoxy groups of another APTES molecule in the presence of a protic solvent that favors the reaction [57]. This is likely a random process, which would explain why the high average hydrodynamic diameters are very different between samples and between the various aliquotes of AS-4 and AS-5 obtained at different times of reaction, assuming that this is mainly related to the self-polymerization of APTES in solution.

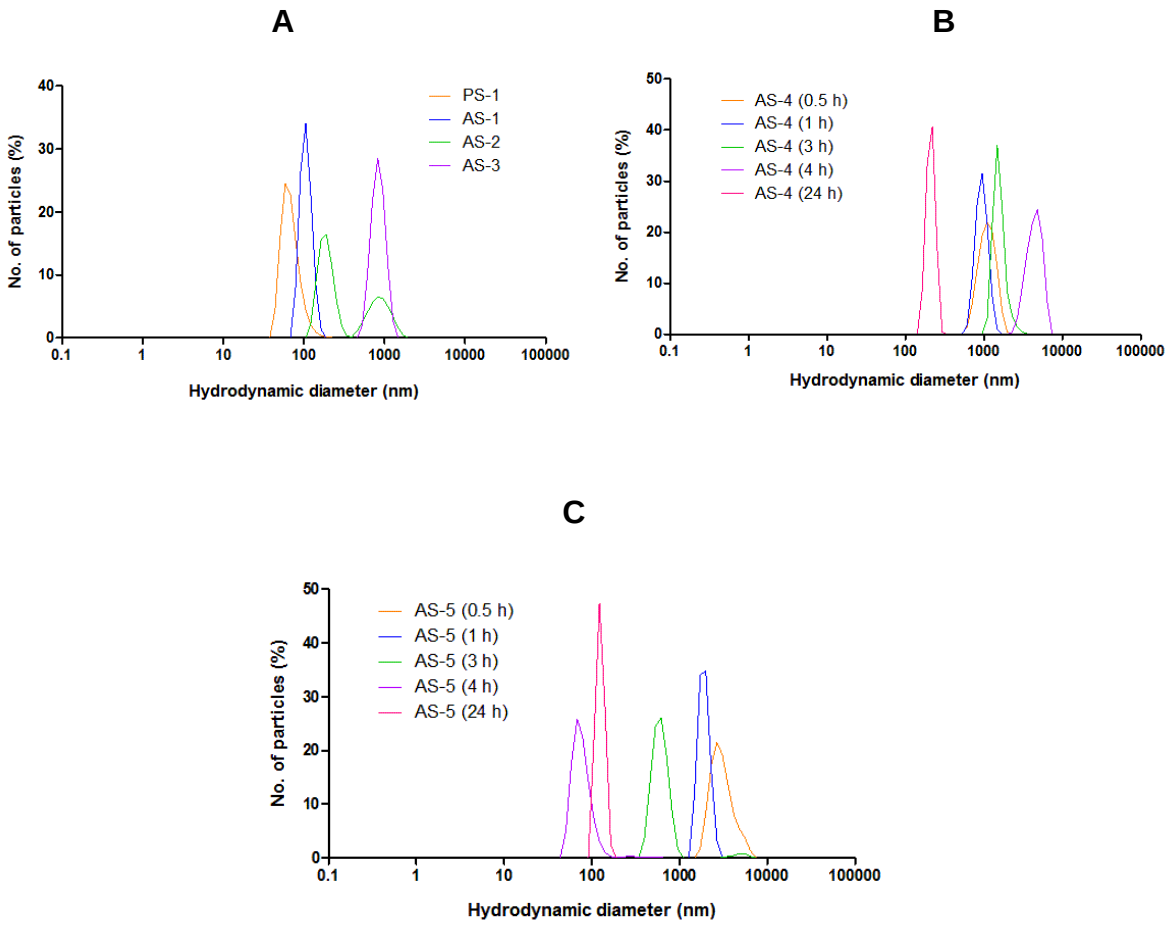

Figure 29 – DLS hydrodynamic diameter distribution (by percentage of number of particles) for: A – plain silica NP batch PS-1 and APTES modified silica NP batches AS-1, AS-2 and AS-3; B – APTES modified silica NP batch AS-4 at different times of removal of aliquots during functionalization reaction; C – APTES modified silica NP batch AS-5 at different times of removal of aliquots during functionalization reaction.

The functionalization in the case of samples AS-2 and AS-3 comprised the addition of water to the absolute ethanol dispersant in a 1:3 volume ratio. It is expected that this

addition provides a greater availability of water molecules that favor the polymer condensation reaction in the solvent, while the non-addition of water in samples AS-1, 4 and 5 would result in a greater tendency to the covalent bonding of APTES to the surface of the NPs due to the probable availability of water molecules adsorbed to the surface. However, the DLS results show no consistent differences between samples functionalized with added water and samples functionalized in absolute ethanol only. Furthermore, the use of $1/10^{th}$ of the amount of APTES in the original protocol in Experiment 5 (sample AS-5) did not result in significant changes in the presence of large particles of various sizes. It was hypothesized that the free self-polymerized APTES originated from the APTES added to the reaction mixture, due to a possible contamination with water. Nevertheless, the use of two different batches of APTES between samples AS-1 and AS-2 did not result in differences on the presence of self-polymerized APTES. However, it is still possible that both batches of APTES were indeed contaminated with water.

The existence of high standard deviations in the DLS size measurements prevents the distinction between free APTES polymer and any APTES that might have been attached to the surface of the NPs. Therefore, the gold decoration of sample AS-3 was attempted to observe whether the surface of the NPs was effectively functionalized with APTES or not.

3.3. Zeta potential measurements

The results for the zeta potential measurements of the APTES functionalized nanoparticle batches are shown in Table 10.

Table 10 – Average zeta potential of APTES functionalized batches (AS) (Experiments 1, 4 and 5 follow the original protocol without addition of water; 2 and 3 include the addition of water at a 1:3 v/v ratio, 5 uses 1/10th of original APTES amount):

Experiment	Parent batch	Average zeta potential (mv)	Batch obtained	Reaction time (hours)	Average zeta potential (mv)
1	PS-1	-28.3 ± 0.7	AS-1	1	-32.6 ± 1.7
2	PS-1	-28.3 ± 0.7	AS-2	1	+13.6 ± 2.3
3	FS-3	-29.8 ± 0.9	AS-3	1	+15.6 ± 1.6
4	FS-4	-29.7±1.4	AS-4	0.5	+13.3 ± 3.2
4	FS-4	-29.7±1.4	AS-4	1	+8.3 ± 3.4
4	FS-4	-29.7±1.4	AS-4	3	+20.5 ± 2.4
4	FS-4	-29.7±1.4	AS-4	4	+17.0 ± 4.2
4	FS-4	-29.7±1.4	AS-4	24	+16.1 ± 2.1
5	FS-4	-29.7±1.4	AS-5	0.5	-7.5 ± 1.2
5	FS-4	-29.7±1.4	AS-5	1	-17.9 ± 3.6
5	FS-4	-29.7±1.4	AS-5	3	-5.7 ± 2.8
5	FS-4	-29.7±1.4	AS-5	4	-16.4 ± 1.6
5	FS-4	-29.7±1.4	AS-5	24	-28.2 ± 2.6

The zeta potential value for sample AS-1 is negative, which may indicate that the NPs were not successfully functionalized and remained the main contributor for the average zeta potential. This sample was functionalized without the addition of water, and it is likely that the absence of water prevented the surface functionalization of AS-1. Both samples AS-2 and AS-3 were functionalized with addition of water to the reaction, thus favoring the condensation reaction between APTES and the silanol groups, and their average zeta potential is positive. The extent to which the NPs themselves were

functionalized is unknown, and it remains a possibility that the positive zeta potential is originated mainly by self-polymerized APTES, although the gold decoration results for AS-3 (discussed in Section 5) support the existence of APTES on the surface of the NPs, and this is likely to have happened in the case of sample AS-2 given that the experimental conditions were the same except for the encapsulation of RITC inside the NPs.

The aliquots of sample AS-4 show a positive average zeta potential, despite the fact that no water was added to the reaction. Given that sample AS-1 did not see a positive change in zeta potential under the same conditions, it is possible that the parent batches of each sample had different amounts of water adsorbed to the surface, thus explaining the different effectiveness of functionalization. The results in Experiment 5 show that all aliquots of sample AS-5 have a negative average zeta potential but higher in comparison with the parent FS-4 batch, and it is known that the amount of APTES added was $1/10^{th}$ of the amount used in all other experiments. Assuming that there was enough water in the parent batch for APTES functionalization, it is likely that the APTES functionalization of the surface of the NPs was incomplete.

The results discussed in this section show that our attempts to modify the RITC-SiNPs with the aminosilane APTES have been unsuccessful in preventing the formation of self-polymerized APTES, which is likely the main cause for the drastic reduction in NP fluorescence. This has motivated us to attempt the surface capping of the RITC-SiNPs with single PAH layers and PAH/PSS multilayers as an alternative for the modification of the surface charge of the RITC-SiNPs, which will be discussed in the following section.

4. Surface capping of RITC-SiNPs with PAH and PSS

4.1. Fluorescence spectroscopy

The fluorimetry spectra of each RITC silica NP batch surface capped with PAH and PAH/PSS multilayers (Figure 30) were acquired in order to check for the effectiveness of RITC fluorescence.

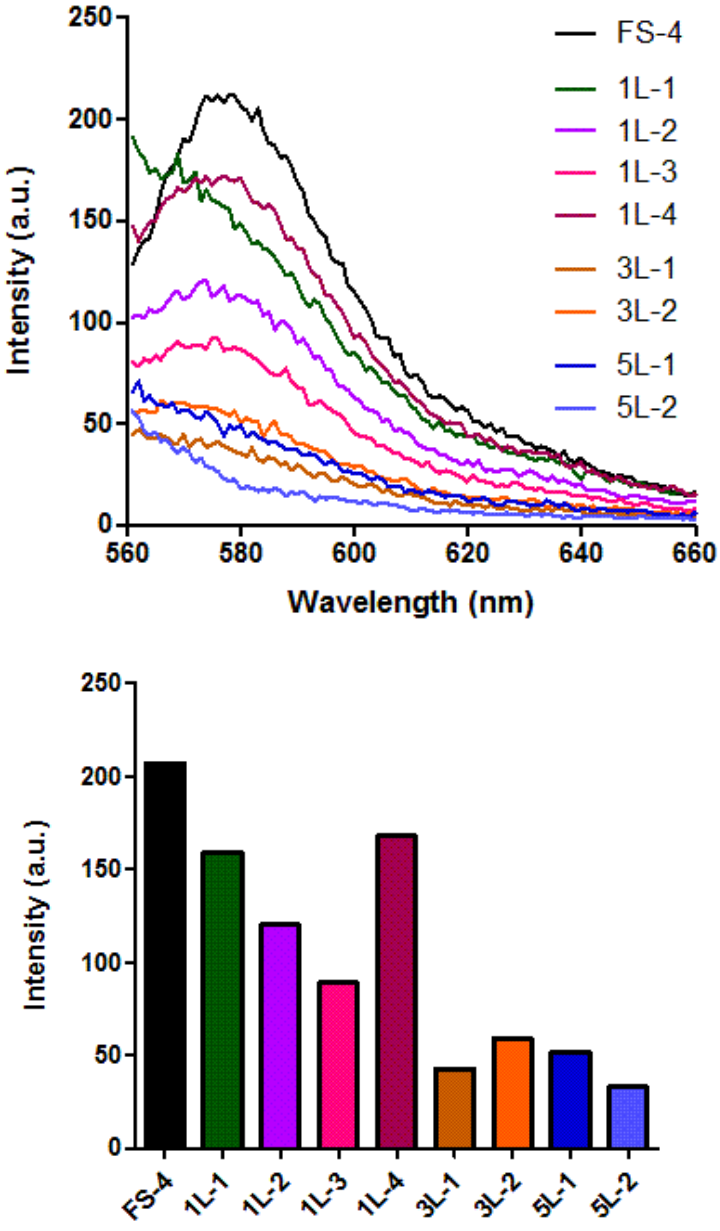

Figure 30 – Fluorescence spectra of PAH-capped RITC-SiNP batches 1L-1 to 4, PAH/PSS 3-layer capped NP batches 3L-1 to 2 and 5-layer capped NP batches 5L-1 and 5L-2, including parent batch FS-4 for comparison purposes.

The results show that the RITC-associated fluorescence is somewhat affected by the PAH capping, and that the sample that was less affected was sample 1L-4; this sample was capped by using a change in methodology consisting in the use of a higher concentration of NaCl, which may have improved the colloidal stability of the PAH during the capping procedure, thus resulting in a layer that is better distributed along the surface of the NPs, which in turn is likely to have resulted in less scattering of the emitted fluorescence by the polymer. The 1L-3 sample was also capped with the same increase in NaCl concentration, but the use of PAH of high molecular weight (Mw ≈ 56000, as opposed to the PAH used in all other cappings with a molecular weight of ca. 15000) may have resulted in higher light scattering of the fluorescence emitted by the RITC. Furthermore, despite the use of more NaCl for colloidal stabilization in the multilayer cappings, the use of multiple layers results in a very significant reduction in sample fluorescence. Interestingly, the fluorescence of the 3L and 5L samples is not very different, indicating that the existence of multiple layers is the main factor of fluorescence reduction, independently of the number of layers. However, it is possible that the successive use of opposite charged polyelectrolytes PAH and PSS resulted in the partial removal of previously NP surface associated polyelectrolytes [45], thus resulting in the similar fluorescence of the 3L and 5L samples; this would also imply that the thickness of the multilayer would be similar for 3L and 5L samples. The removal of opposite charged polyelectrolytes in a layer-by-layer surface coating with PAH and PSS has been observed in a study by Smith et al. [45]. In this study it was shown that the subsequent application of PAH to a PSS outer layer or vice-versa resulted in significant losses of the outermost polyelectrolyte. Another possibility is that the fluorescence of the multilayer samples is not due to RITC but to scattering by the polymers, as in the case of the APTES functionalized samples (Section 3).

4.2. Dynamic Light Scattering (DLS)

The DLS size measurement results for the PAH and PAH/PSS multilayer surface capped FS-4 RITC-SiNPs are shown in Table 11, and the hydrodynamic diameter distributions are shown in Figure 31.

Table 11 – Average hydrodynamic diameter of PAH and PAH/PSS multilayer capped RITC-SiNP batches (FS-4 parent batch average hydrodynamic diameter = 70 ± 16 nm):

Batches	Average hydrodynamic diameter (nm)
1L-1	153 ± 123
1L-2	388 ± 75
1L-3	673 ± 218
1L-4	91 ± 8.1
3L-1	140 ± 25
3L-2	133 ± 17
5L-1	177 ± 46
5L-2	142 ± 32

The results show that the first three 1L batches have high hydrodynamic diameters in comparison with the FS-4 parent batch. 1L-1 and 1L-2 samples are likely to present free polymer or disorganized layers on the surface of the NPs, which is in agreement with the hypothesis that the use of less NaCl may have resulted in reduced colloidal stability of the PAH polymer and a greater tendency to remain dissociated from the NP surface or form uneven layers around it. Sample 1L-3 was capped with PAH with a much greater molecular weight (Mw ≈ 56000) which has likely formed polymer agglomerates free in solution and thus contributes to the high hydrodynamic diameter average and standard deviation of the sample. In contrast, sample 1L-4 shows an average hydrodynamic diameter in agreement with an effective and well distributed PAH capping of FS-4, thus prompting the use of the same parameters in the multilayer capping with PAH. As the number of polymer layers increases, the 3L and 5L samples show an increase in average hydrodynamic diameter, which is in agreement with the expected increase both in size

and solvent that moves together with the NPs due to the larger surface exposed with the charged amino groups of the PAH polymer.

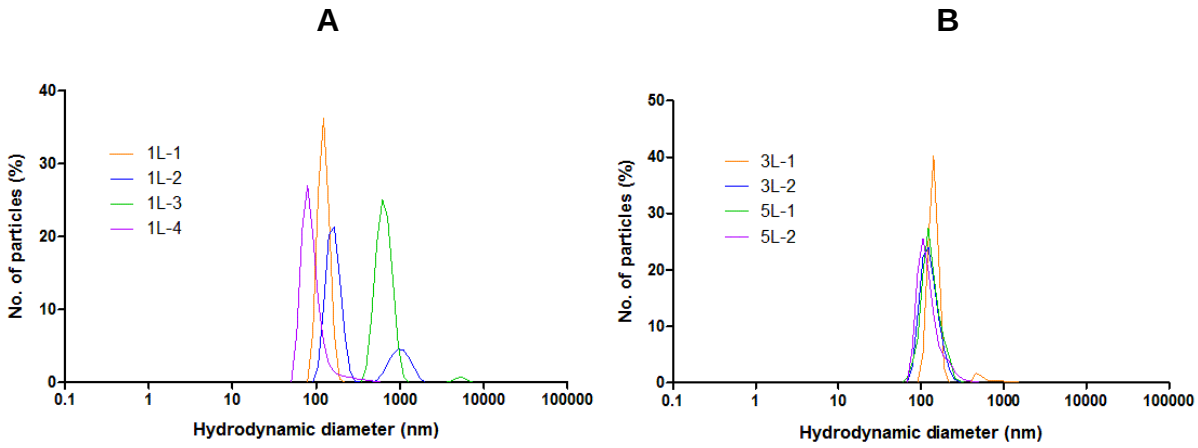

Figure 31 – DLS hydrodynamic diameter distribution (by percentage of number of particles) for: A – PAH-capped silica NP batches 1L-1 to 4; B – PAH/PSS 3-layer-capped silica NP batches 3L-1 and 3L-2 and 5-layer-capped silica NP batches 5L-1 and 5L-2.

4.3. Zeta potential measurements

The results for the zeta potential measurements of the RITC-SiNP batches are shown in Table 12. Samples 1L-1 and 1L-2 show a slightly negative average zeta potential, which is in agreement with the hypothesis that the surface capping in these samples was affected by a reduced colloidal stability of the polymer due to low ionic strength. In contrast, the single-layer samples 1L-3 and 1L-4 show a reasonably positive zeta potential average, which is consistent with a surface modification that does not completely cover the whole surface of the NPs, assuming that the total covering would imply higher zeta potential absolute values, as in the case of the 3L samples.

Table 12 – Average zeta potential of PAH and PAH/PSS multilayer capped RITC-SiNP batches (FS-4 parent batch average zeta potential = -29.7 ± 1.4 mV):

Batches	Average zeta potential (mV)
1L-1	-7.5 ± 0.1
1L-2	-2.3 ± 1.2
1L-3	+11.3 ± 2.7
1L-4	+15.2 ± 1.1
3L-1	+43.3 ± 2.5
3L-2	+40.6 ± 1.8
5L-1	+21.6 ± 3.2
5L-2	+27.3 ± 1.2

The 5L samples show lower zeta potential values in comparison with the 3L samples, which is in agreement with the possibility of partial removal of polyelectrolyte layers by the opposite charged polymer as observed by Smith et al. [45].

5. Gold decoration of RITC-doped silica nanoparticles

5.1. UV-Vis spectroscopy

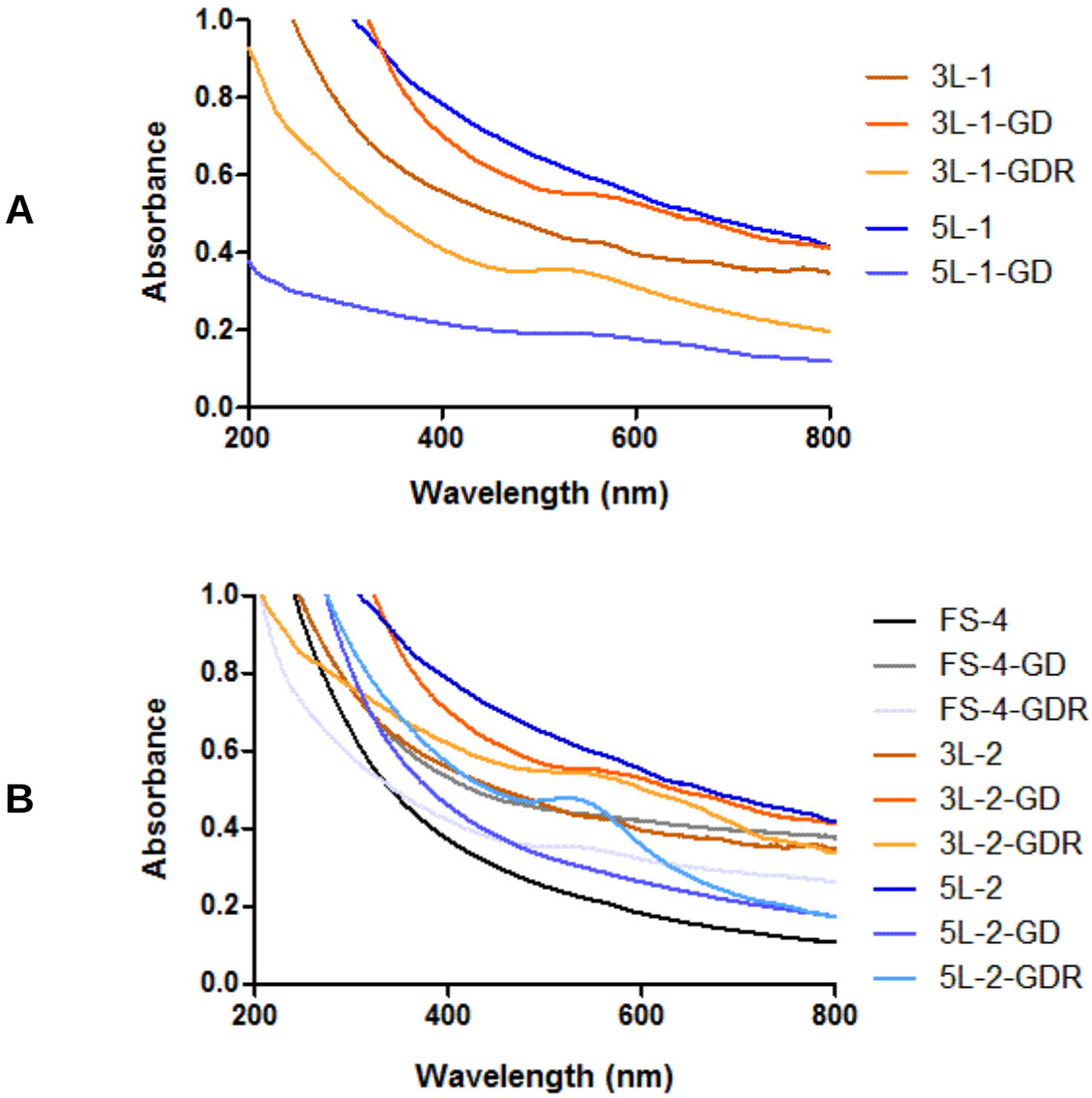

Figure 32 – UV-Vis spectra of: A - gold decorated NP batches 3L-1-GD and 5L-1-GD, including reduced version 3L-1-GDR and parent batches 3L-1, 5L-1 and FS-4; B – gold decorated NP batches (decorated using one-tenth of the original concentration of gold (III) chloride) FS-4-GD, 3L-2-GD and 5L-2-GD, including their respective reduced versions and parent batches FS-4, 3L-2 and 5L-2.

The UV-Vis results for the first set of gold decorated NPs (Figure 32-A) show that the gold decorated samples present a broad absorption band between 530 and 630 nm of

wavelength, which is in agreement with the presence of gold in the samples. However, these results are inconclusive given that the aforementioned bands are small in intensity. The reduced samples show similar absorption bands in comparison with the non-reduced samples, which is likely due to the possibility that a significant number of gold hydroxide nanoclusters was already reduced before the addition of sodium borohydrate. In the second set of gold decorated NPs (Figure 32-B) the gold decorated samples FS-4-GD and 5L-2-GD do not show a defined absorption band characteristic of the presence of gold, which may indicate the unsuccessful gold decoration of the NPs. After reduction with sodium borohydrate, these samples present absorption related to the presence of reduced gold, which may have originated from unbound gold hydroxide. In contrast, the 3L-2 derived gold decorated samples 3L-2-GD and 3L-2-GDR show the expected absorption bands for gold nanoclusters.

The AS-3-GD and AS-3-GDR samples are not shown due to the unavailability of sufficient sample material for UV-Vis spectroscopy.

5.2. Fluorescence spectroscopy

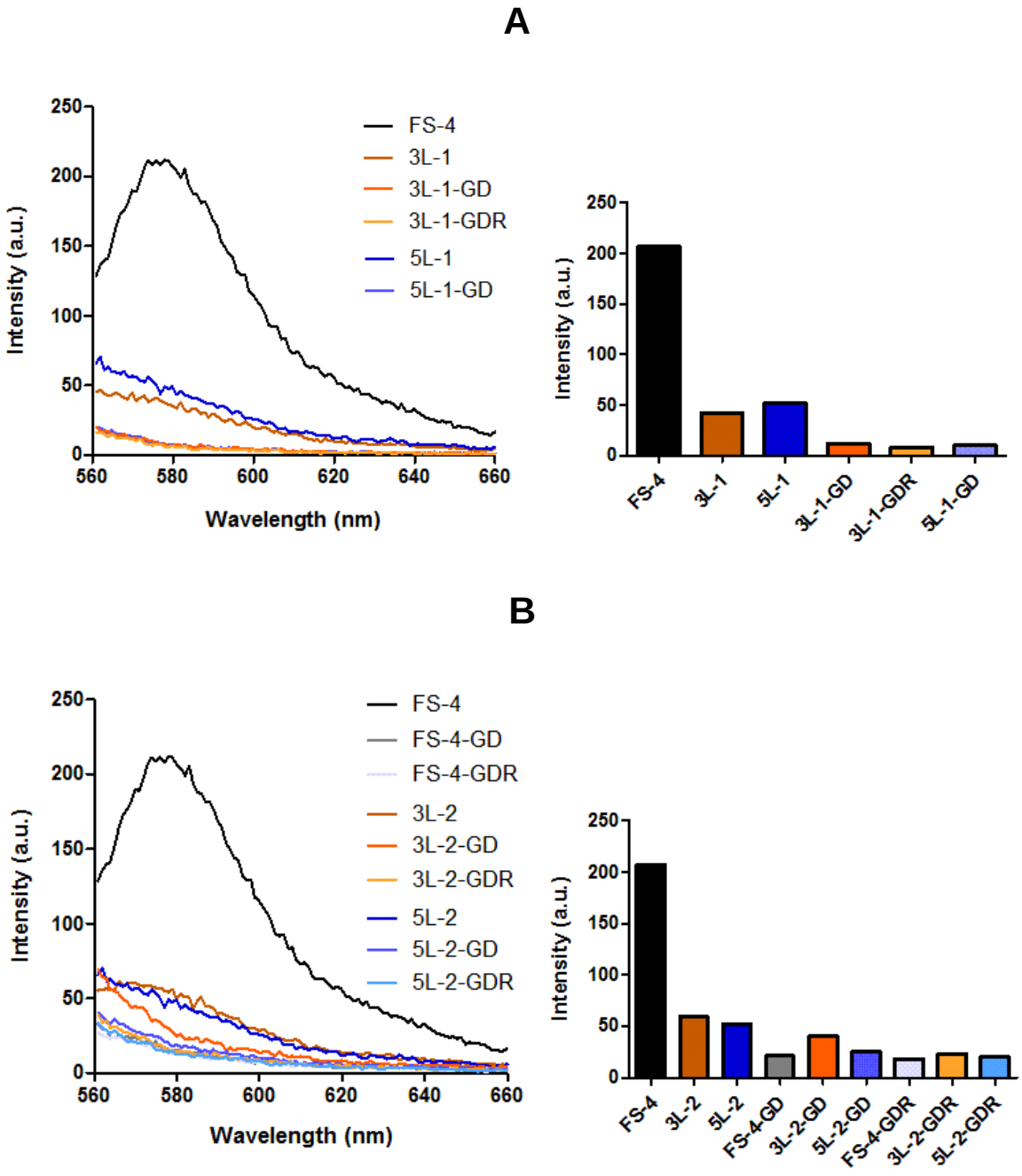

Figure 33 – Fluorescence spectra of: A- gold decorated NP batches 3L-1-GD and 5L-1-GD, including reduced version 3L-1-GDR and parent batches 3L-1, 5L-1 and FS-4; B – gold decorated NP batches (decorated with one-tenth of the original concentration of gold (III) chloride) . FS-4-GD, 3L-2-GD and 5L-2-GD, including their respective reduced versions and parent batches FS-4, 3L-2 and 5L-2.

Both the first set (Figure 33-A) and the second set of gold decorations (Figure 33-B) consistently show a significant reduction in fluorescence after gold decoration. This

could be due to significant quenching of the RITC-derived fluorescence by either gold associated to the surface of the NPs or gold present in solution; unfortunately, a distinction between these two possible causes is not possible by using the results here presented. It is also observable that the reduction in fluorescence is higher in the reduced samples, which is expectable since the size and number of reduced gold particles (whether free in solution or associated to the NPs) should increase after reduction with sodium borohydrate. The AS-3-GD and AS-3-GDR samples are not shown due to the unavailability of sufficient sample material for fluorescence spectroscopy.

5.3. Transmission Electron Microscopy

TEM images of the AS-3-GD and AS-3-GDR samples are shown in Figure 34.

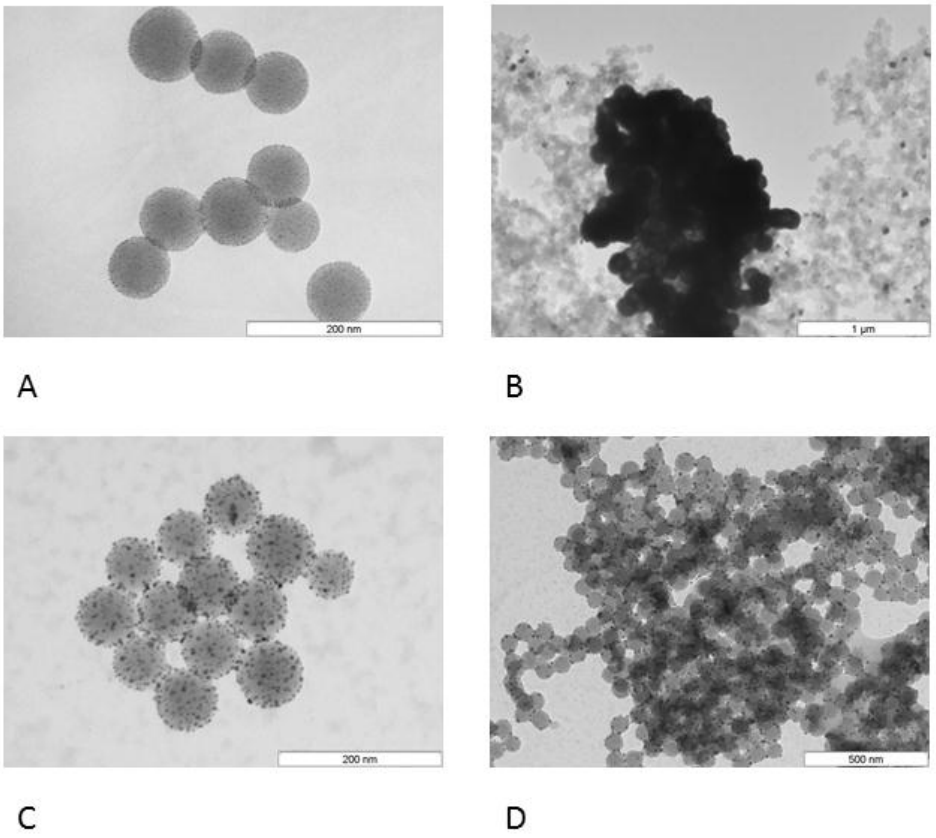

Figure 34 – TEM images of gold decorated samples AS-3-GD (A and B) and AS-3-GDR (C and D).

The presence of gold nanoclusters on the surface of the NPs is visible in both samples, and the size of the gold nanoclusters is increased in the case of the reduced sample. Sample AS-3-GD shows the presence of large agglomerates of gold particles that may be related to an excess of gold, and is one of the results that prompted the attempt to use less gold in the aforementioned second set of gold decorations. However, the AS-3-GDR sample does not present any large agglomerates of gold, and this might be due to an effective washing of the sample after reduction with sodium borohydrate. These results suggest that the APTES functionalization of the NP surface did result in the formation of an APTES layer on the surface, despite the existence of free APTES polymer discussed in Section 3. This is also corroborated by the ineffectiveness of the gold decoration carried with RITC-SiNPs without any functionalization of the surface, which will be discussed later in this section.

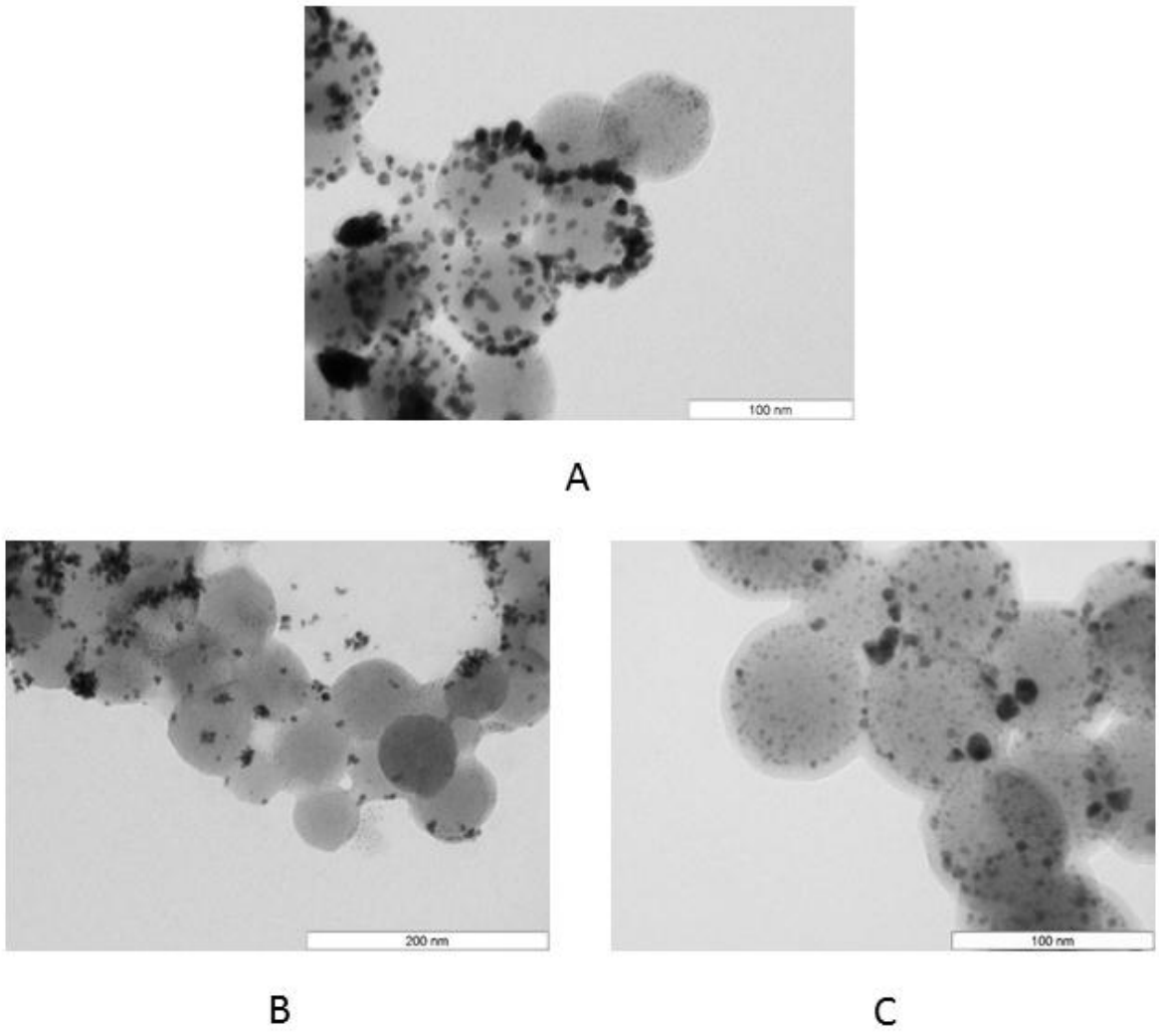

Figure 35 – TEM images of gold decorated samples 3L-1-GD (A), 3L-1-GDR (B) and 5L-1-GD (C).

Samples 3L-1-GD and 3L-1-GDR (Figure 35-A and B) show an uneven gold decoration of the NPs. A possibility that may explain this is an uneven distribution of surface charge after capping with the multilayer of PAH/PSS, given that the opposite charged polymers may partially remove the surface bound polymers instead of forming a superimposed layer around the surface of the NPs, as discussed in Section 4. In contrast, sample 5L-1-GD (Figure 35-C) shows a well-distributed gold decoration around the NPs; it is possible that the successive capping with PAH and PSS further compensates for the previous removal of surface-bound polyelectrolytes, thus resulting in a greater homogeneity of surface charge, which would in turn provide better conditions for an even distribution of the gold seeding.

The TEM images of the multilayered samples also show the presence of a contour around the surface of the NPs which is likely to represent the polyelectrolyte multilayer, thus providing further indication that the multilayer capping occurred in those samples. However, Figure 35-C shows that the gold decoration is inside this contour, and it is uncertain whether the gold decoration establishes itself in the NP surface instead of the PAH/PSS multilayer or if the contour is actually the multilayer and not an unknown contaminant.

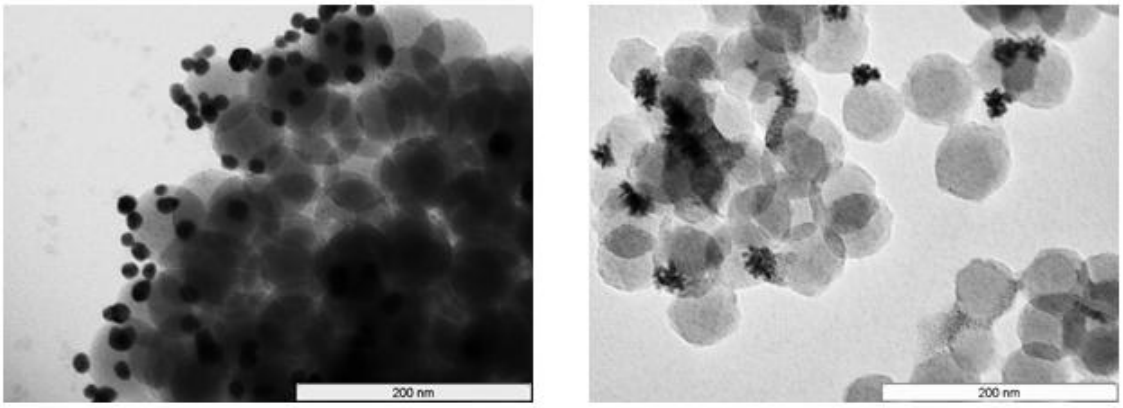

Figure 36 – TEM images of gold decorated samples FS-4-GD (A) and 5L-2-GD (B).

The RITC-SiNP sample FS-4 is expected to be inadequate for gold decoration due to the predominance of negative charges at the surface [39], and the TEM results for sample FS-4-GD (Figure 36-A) show that the gold decoration was not effective, thus confirming that the RITC-SiNPs require further modification before gold decoration.

Sample 5L-2-GD (Figure 36-B) also presents an ineffective gold decoration. The existence of gold nanoclusters agglomerated in certain surface regions of the NPs is

observable, and this may be related to an uneven charge distribution due to a reduced homogeneity of the PAH/PSS multilayer. In addition, the presence of a lighter-coloured layer around the surface of the NPs is observable, and it is likely that this layer represents the polyelectrolyte multilayer, given that the heavier elements in the silica network are expected to scatter electrons more than the lighter elements present in the polyelectrolytes.

5.4. Dynamic Light Scattering (DLS)

Table 13 – Average hydrodynamic diameter of gold decorated NP batches:

Parent batch	Average hydrodynamic diameter (nm)	Gold decorated	Average hydrodynamic diameter (nm)	Reduced	Average hydrodynamic diameter (nm)
3L-1	140 ± 25	3L-1-GD	152 ± 45	3L-1-GDR	167 ± 103
5L-1	177 ± 46	5L-1-GD	165 ± 32		
AS-3	733 ± 210	AS-3-GD	107 ± 67	AS-3-GDR	80 ± 29
FS-4	70 ± 16	FS-4-GD	102 ± 78	FS-4-GDR	112 ± 180
3L-2	133 ± 17	3L-2-GD	147 ± 18	3L-2-GDR	203 ± 32
5L-2	142 ± 32	5L-2-GD	207 ± 56	5L-2-GDR	192 ± 87

The DLS size measurement results for the gold decorated and reduced NP samples are shown in Table 13, and the hydrodynamic size distributions for these samples are shown in Figure 37. Samples originated from 3L-1 and 5L-1 show values that are consistent with the absence of large gold particles, thus allowing us to conclude that the washing of excess gold was effective. In turn, samples originated from AS-3 APTES modified NPs show hydrodynamic diameter values that indicate the removal of large particles such as free APTES polymer after gold decoration; however, these results are in disagreement with the TEM images obtained for this sample (Figure 34) that reveal the existence of large gold agglomerates. In contrast, the results for the reduced version (AS-3-GDR) are in agreement with the absence of large particles seen in the TEM images (Figure 34).

Gold decorated samples originated from FS-4 show increasing hydrodynamic diameters, which are likely due to the presence of gold nanoclusters of greater than

average size observed in the TEM results. The samples originated from 3L-2 and 5L-2 also show increasing hydrodynamic diameters along the gold seeding and reduction steps, and standard deviations are not very significant; this is in agreement with the absence of excess gold to form large particles, which may be related to an effective washing of excess gold or to the use of 1/10th of the amount of gold originally used in the first set of experiments.

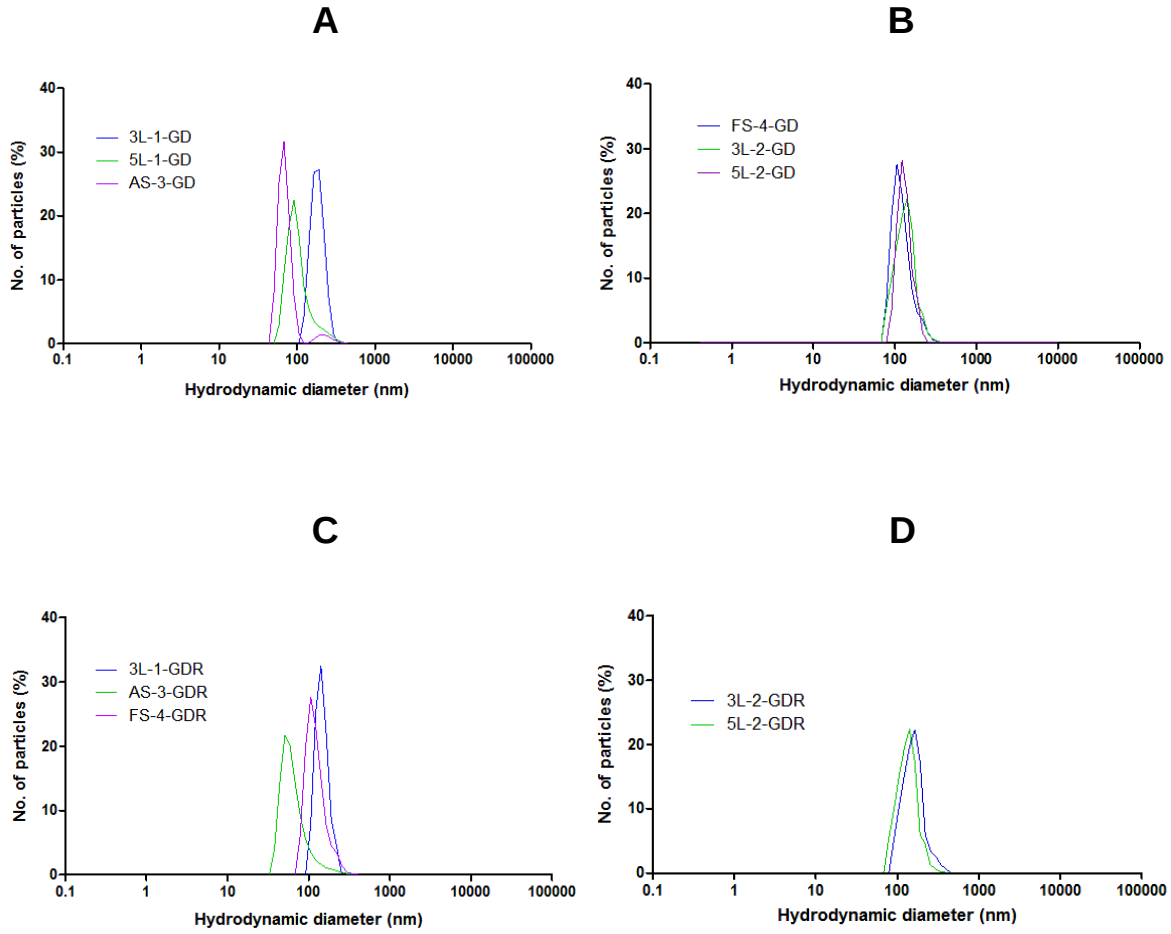

Figure 37 – DLS hydrodynamic diameter distribution (by percentage of number of particles) for: A and B – gold decorated silica NP batches; C and D – gold decorated silica NP batches subjected to reduction by sodium borohydrate.

5.5. Zeta potential measurements

The results for the zeta potential measurements of the gold decorated batches are shown in Table 14.

Table 14 – Average zeta potential of gold decorated NP batches:

Parent batch	Average zeta potential (mV)	Gold decorated	Average zeta potential (mV)	Reduced	Average zeta potential (mV)
3L-1	+43.3 ± 2.5	3L-1-GD	+14.4 ± 2.3	3L-1-GDR	+29.7 ± 1.8
5L-1	+21.6 ± 3.2	5L-1-GD	+16.5 ± 2.7		
AS-3	+15.6 ± 1.6	AS-3-GD	+1.2 ± 2.2	AS-3-GDR	+7.5 ± 2.4
FS-4	-29.7±1.4	FS-4-GD	-30.7 ± 1.2	FS-4-GDR	-26.7 ± 2.3
3L-2	+40.6 ± 1.8	3L-2-GD	+12.8 ± 1.9	3L-2-GDR	+22.8 ± 0.7
5L-2	+27.3 ± 1.2	5L-2-GD	+24.6 ± 1.3	5L-2-GDR	+22.6 ± 3.0

The PAH/PSS multilayered batches show in general the decrease of the initially positive zeta potential conferred by the outer PAH layer after the addition of gold hydroxide, and an increase of zeta potential after reduction that may be related to the reduction of the gold hydroxide and consequent neutralization of its negative charge. In turn, sample AS-3 also suffers a decrease in zeta potential after gold decoration, and an increase after reduction with sodium borohydrate, which is expected as previously discussed.

Chapter IV

Conclusions and Outlook

The first main objective of this work was to achieve the synthesis of RITC-doped silica nanoparticles with a successful encapsulation of the RITC fluorophore, dispersion stability, good size dispersion and an unimpeded silica surface for further modification. Therefore, various characterization techniques were used in order to check for these requirements. UV-Vis spectroscopy was used to screen for the absorption band specific for the absorption of light by the RITC fluorophore; however, some samples did not clearly show this band, therefore the fluorescence spectroscopy of the RITC-SiNPs was crucial in confirming the existence of RITC-derived fluorescence, which was successfully detected in all samples. Furthermore, in order to check for the stability of the dispersion, we have used a fluorimetry-based assay to evaluate the sedimentation rate of the RITC-SiNPs, which allowed us to conclude that the dispersion stability of the NPs is only compromised after several minutes without any agitation. The size of the RITC-SiNPs was studied by TEM, AFM and DLS size measurements, which allowed us to conclude that these nanoparticles have a reasonably narrow size dispersion that allows the further design of biosensors with a consistent size. Zeta potential measurements have provided useful data in monitoring the surface charge of the NPs, thus allowing the gathering of data related to the overall chemical composition of the surface of the NPs. In conclusion, the results obtained in the experimental work show that the synthesized RITC-SiNPs meet the requirements for providing a fluorescent platform for the design of novel biosensors.

Another main goal of the present work was to achieve the successful functionalization of RITC-SiNPs with GPTMS as a linker for thiolated oligonucleotides, thus obtaining platform for building a novel fluorescent biosensor for the sequence-specific detection of DNA. The results obtained during the experimental work show that the functionalization with GPTMS was successful, providing fluorescent nanoparticles with a stable surface modification. The GPTMS functionalized samples were studied by many of the methodologies used for characterizing the RITC-SiNP batches in order to follow the success of the functionalization and to check whether the capabilities presented by the RITC-SiNPs were still present after functionalization. The results for these characterization techniques are in agreement with a successful functionalization using the selected methodology. Furthermore, the stability of the epoxide ring intended for linking oligonucleotides to the NPs was shown to be optimal in the experimental conditions to which the samples were subjected, thus adding to the robustness of the biosensor platform. The use of ^{1}H NMR was crucial for obtaining this information, and its usefulness in confirming the functionalization of silica surface with organosilanes was successfully proven in the present work. On the other hand, the use of FTIR and DRIFTS to confirm

the presence of the GPTMS epoxide was shown to be ineffective given the presence of strong peaks coinciding with the characteristic absorption region of the epoxide ring.

The present work also had as an objective the gold decoration of RITC-SiNPs for obtaining a multifunctional biosensor platform that combines both fluorescence and plasmonic-based absorption for the detection of specific gene sequences. Since the gold decoration of the NPs is known to require the neutralization of the negative charge at the surface of the NPs, the functionalization with the aminosilane APTES was studied. The results show that the APTES functionalization did provide an effective surface modification for the gold decoration by a deposition-precipitation method; however, the presence of self-polymerized APTES in solution resulted in the significant reduction of NP fluorescence. This was not overcome by the various attempts made towards optimization of the functionalization protocol, thus prompting the study of a different strategy to achieve surface preparedness for gold decoration by using the polyelectrolytes PAH and PSS to create single and multilayered polymer coatings associated to the surface of the RITC-SiNPs. However, the fluorescence of the NPs was shown to be reduced by using multilayered coatings, and the gold decoration of both single and multilayer coated NPs resulted in the drastic reduction of their fluorescence.

Both UV-Vis and fluorescence spectrometries have shown differences in signal intensity between samples with a known mass concentration, and the causes for these differences remain unknown. These differences have prevented the use of these two methodologies for quantification of the NPs, and future work in the characterization of the RITC-SiNPs and their surface modified versions should be carried in order to provide an effective methodology for the quantification of the NPs and to obtain information about the causes for the aforementioned differences in signal intensity.

It also remains unclear whether the reduction in the fluorescence of the gold decorated NPs is mainly due to quenching by the gold nanoclusters adhered to the surface of the NPs or due to the presence of gold free in solution, and further studies should be carried in order to obtain information that may discriminate between these possible causes.

References

[1] B.D. Malhotra, R. Singhal, A. Chaubey, S.K. Sharma, A. Kumar, “Recent trends in biosensors”, *Current Applied Physics* **2005,** *5* (2), 92–97.

[2] S.P.J. Higson, S.M. Reddy, P.M. Vadgama, “Enzyme and other biosensors: evolution of a technology”, *Engineering Science and Education Journal* **1994**, *3*, 41–48.

[3] S. P. Mohanty, E. Kougianos, “Biosensors: a tutorial review”, *IEEE Potentials* **2006**, *25* (2), 35-40.

[4] L. M. Bellan, D. Wu, R. S. Langer, “Current trends in nanobiosensor technology”, *Wiley Nanomed* **2011**, *3*, 229-246.

[5] K. E. Sapsford, K. M. Tyner, B. J. Dair, J. R. Deschamps, I. L. Medintz, “Analyzing nanomaterial bioconjugates: a review of current and emerging purification and characterization techniques”, *Analytical Chemistry* **2011**, *83*, 4453-4488.

[6] A. D’Amico, C. Di Natale, “A contribution on some basic definitions of sensors properties”, *IEEE Sensors Journal* **2001**, *1*, 183–190.

[7] X. Fan, I. M. White, S. I. Shopova, H. Zhu, J. D. Suter, Y. Sun, “Sensitive optical biosensors for unlabeled targets: A review”, *Analytica Chimica Acta* **2008**, *620* (1-2), 8-26.

[8] X. D. Hoa, A. G. Kirk, M. Tabrizian, “Towards integrated and sensitive surface plasmon resonance biosensors: A review of recent progress”, *Biosensors & Bioelectronics* **2007**, *23* (2), 151-160.

[9] M. C. Desjonqueres *et al.*, *Concepts in surface physics*, **1993**, Springer-Verlag.

[10] J. V. Veetil, K. Ye, “Development of immunosensors using carbon nanotubes”, *Biotechnology Progress* **2008**, *23*, 517–531.

[11] H. Ai, S. A. Jones, Y. M. Lvov, “Biomedical applications of electrostatic layer-by-layer nano-assembly of polymers, enzymes, and nanoparticles” *Cell Biochemistry and Biophysics* **2003**, *39* (1), 23-43.

[12] J. A. Howarter, J. P. Youngblood, “Optimization of silica silanization by 3-aminopropyltriethoxysilane”, *Langmuir* **2006**, *22*, 11142–11147.

[13] D. Zhang, E.C. Alocilja, “Characterization of nano-porous silicon-based DNA biosensor for the detection of salmonella enteritidis”, *IEEE Sensors. Journal* **2008**, *8*, 775–780.

[14] M. Tichoniuk, M. Ligaj, M. Filipiak, “Application of DNA hybridization biosensor as a screening method for the detection of genetically modified food components”, *Sensors* **2008**, *8*, 2118–2135.

[15] L. B. Hendry, V. B. Mahesh, E. D. Bransome, D. E. Ewing, "Small molecule intercalation with double stranded DNA: Implication for normal gene regulation and for predicting the biological efficacy and genotoxicity of drugs and other chemicals", *Mutation Research/Fundamental and Molecular Mechanisms* **2007**, *623*, 53-71.

[16] L. Verschaeve, G. Koppen, U. van Gorp, G. Schoeters, G. Jacobs, C. Zwijzen, "Seasonal variations in spontaneous levels of DNA damage: implications in the risk assessment of environmental chemicals", *Journal of Applied Toxicology* **2007**, *27*, 612–620.

[17] C. Hempen, U. Karst, "Labeling strategies for bioassays", *Anaytical and Bioanalytical Chemistry* **2005**, *384*, 572–583.

[18] Y. Yamamoto, "PCR in diagnosis of infection: detection of bacteria in cerebrospinal fluids", *Clinical and Vaccine Immunology* **2002**, *9*, 508.

[19] X. Kai, H. Junran, Y. Zunzhong, Y. Yibin, L. Yanbin, "Recent development of nano-materials used in DNA biosensors", *Sensors* **2009**, *9*, 5534-5557.

[20] L. Dong-Eun, K. Heeboom, S. In-Cheol, R. H. Ju, K. Kwangmeyung, C. K. Ick, "Multifunctional nanoparticles for multimodal imaging and theragnosis", *Chemical Society Reviews* **2012**, *41*, 2656-2672.

[21] G. Schottner, "Hybrid sol-gel-derived polymers: applications of multifunctional materials", *Chemistry of Materials* **2001**, *13*, 3422–3435.

[22] K. H. Haas, "Hybrid inorganic-organic polymers based on organically modified Si-alkoxides", *Advanced Engineering Materials* **2000**, *2*, 571–582.

[23] L. Jinhuai, L. Jinyun, Y. Liangbao, C. Xing, Z. Meiyun, M. Fanli, L. Tan, L. Minqiang, "Nanomaterial-assisted signal enhancement of hybridization for DNA biosensors: a review", *Sensors* **2009**, *9* (9), 7343-7364.

[24] L. Bau, P. Tecilla, F. Mancin, "Sensing with fluorescent nanoparticles", *Nanoscale* **2011**, *3*(1), 121–133.

[25] N. J. Wittenberg, C. L. Haynes, "Using nanoparticles to push the limits of detection", *WIREs Nanomedicine and Nanobiotechnology* **2009**, 1(2), 237–254.

[26] B. Andrew, O. Hooisweng, W. Ulrich, "Fluorescent core-shell silica nanoparticles: towards "Lab on a Particle" architectures for nanobiotechnology", *Chemical Society Reviews* **2006**, *35*, 1028-1042.

[27] H. Ow, D. Larson, M. Srivastava, B. Baird, W. Webb, U. Wiesner, "Bright and stable core-shell fluorescent silica nanoparticles", *Nano Letters* **2005**, *5*, 113–117.

[28] W. Stöber, A. Fink, E. Bohn, "Controlled growth of monodisperse silica spheres in the micron size range", *Journal of Colloid and Interface Science* **1968**, *26*, 62-69.

[29] R. P. Bagwe, C. Yang, L. R. Hilliard, W. Tan, “Surface modification of silica nanoparticles to reduce aggregation and non-specific binding”, *Langmuir* **2004**, *20*, 8336-8342.

[30] A. Aurélien, S. Jorice, P. Olivier, R. Olivier, “A comparative study of non-covalent encapsulation methods for organic dyes into silica nanoparticles”, *Nanoscale Research Letters* **2011**, *6* (1), 1-12.

[31] F. J. Arriagada, K. Osseo-Asare, “Synthesis of nanosize silica in a nonionic water-in-oil microemulsion: effects of the water/surfactant molar ratio and ammonia concentration”, *Journal of Colloid and Interface Science* **1999**, *211*, 210-220.

[32] L. Wang, K. Wang, S. Santra, X. Zhao, L. Hilliard, J. Smith, Y. Wu, W. Tan, “Watching silica nanoparticles glow in the biological world”, *Analytical Chemistry* **2006**, *78*, 646-654.

[33] S. Mahajan, D. Sethi, S. Seth, A. Kumar, P. Kumar, K. C. Gupta, “Construction of oligonucleotide microarray (Biochip) via thiolether linkage for the detection of bacterial meningitis”, *Bioconjugate Chemistry* **2009**, *20*, 1703-1710.

[34] T. Biver, N. Eltugral, A. Pucci, G. Ruggeri, A. Schena, F. Secco, M. Venturini, “Synthesis, characterization, DNA interaction and potential applications of gold nanoparticles functionalized with Acridine Orange fluorophores”, *Dalton Transactions* **2011**, *40* (16), 4190-4199.

[35] C. Graf, A. van Blaaderen, “Metallodielectric colloidal core-shell particles for photonic applications”, *Langmuir* **2002**, *18* (2), 524-534.

[36] T. Pham, *et al.,* “Preparation and characterization of gold nanoshells coated with self-assembled monolayers”, *Langmuir* **2002**, *18* (12), 4915-4920.

[37] W. L. Shi, *et al.*, “Gold nanoshells on polystyrene cores for control of surface plasmon resonance”, *Langmuir* **2005**, *21*(4), 1610-1617.

[38] L. Prati, G. Martra, “New gold catalysts for liquid phase oxidation”, *Gold Bulletin* **1999**, *32* (3), 96-101.

[39] M. Haruta, “Nanoparticulate gold catalysts for low-temperature CO oxidation”, *Journal of New Materials for Electrochemical Systems* **2004**, *7* (3) 163-172.

[40] J. C. Y. Kah, N. Phonthammachai, R.C. Y. Wan, J. Song, T. White, S. Mhaisalkar, I. Ahmad, C. Sheppard, M. Olivo, “Synthesis of gold nanoshells based on the deposition-precipitation process”, *Gold Bulletin* **2008**, *41* (1), 23-36.

[41] C. D. Maule, P. Quaresma, P. A. Carvalho, P. Jorge, E. Pereira, C. C. Rosa, “Nanoparticles for enhanced contrast optical coherence tomography”, *Proceedings of SPIE* **2008**, *7139*, 71390V.

[42] E. Dulkeith, A. C. Morteani, T. Niedereichholz, T. A. Klar, J. Feldmann, “Fluorescence quenching of dye molecules near gold nanoparticles: radiative and nonradiative effects”, *Physical Review Letters* **2002**, *89* (20), 203002-203006.

[43] K. A. Kang, J. Wang, J. B. Jasinski, S. Achilefu, “Fluorescence manipulation by gold nanoparticles: from complete quenching to extensive enhancement”, *Journal of Nanobiotechnology* **2011**, *9*, 16-29.

[44] K. Ray, R. Badugu, J. R. Lakowicz, “Polyelectrolyte layer-by-layer assembly to control the distance between fluorophores and plasmonic nanostructures”, *Chemistry of Materials* **2007**, *19*, 5902-5909.

[45] R. N. Smith, M. McCormick, C. J. Barrett, L. Reven, H. W. Spiess, “NMR studies of PAH/PSS polyelectrolyte multilayers adsorbed onto silica”, *Macromolecules* **2004**, *37*, 4830-4838.

[46] D. A. Skoog, *Principles of Instrumental Analysis (6th ed.)* **2007**, *Thomson Brooks/Cole*.

[47] J. R. Lakowicz, *Principles of Fluorescence Spectroscopy* **1999**, *Kluwer Academic/Plenum Publishers.*

[48] C. N. R. Rao, K. Biswas, “Characterization of nanomaterials by physical methods”, *Annual Review of Analytical Chemistry* **2009**, *2*, 435-462.

[49] B. J. Berne, R. Pecora, *Dynamic Light Scattering With Applications to Chemistry, Biology, and Physics,* **2000**, *Dover Publications*.

[50] A. V. Delgado; F. Gonzalez-Caballero; R. J. Hunter; L. K. Koopal; J. Lyklema, “Measurement and interpretation of electrokinetic phenomena”, *Pure And Applied Chemistry* **2005**, *77* (10), 1753-1850.

[51] P. Eaton, P. West, *Atomic Force Microscopy*, **2010**, *Oxford*.

[52] D. H. Williams, I. Fleming, *Spectroscopic Methods in Organic Chemistry (5th ed.),* **1995**, *McGraw-Hill*.

[53] K. W. Raymond, J. A. Corkill, “Diffuse reflectance infra-red spectrometry”, *Journal of Chemical Education* **1994**, *71* (8), A204.

[54] I. C. P. Smith, D. E. Blandford, “Nuclear magnetic resonance spectroscopy”, *Analytical Chemistry* **1995**, *67* (12), 509–518.

[55] Y. Nakahara, T. Takeuchi, S. Yokoyama, K. Kimura, “Quantitative 1H NMR analysis of reacted silanol groups in silica nanoparticles chemically modified with monochlorosilanes”, *Surface and Interface Analysis* **2010**, *43*, 809-815.

[56] S. Rüdiger, S. M. V. Freund, D. B. Veprintsev, A. R. Fersht, CRINEPT-TROSY NMR reveals p53 core domain bound in an unfolded form to the chaperone Hsp90”, *PNAS* **2002**, *99* (17), 11085-11090.

[57] S. Oh, T. Kang, H. Kim, J. Moon, S. Hong, J. Yi, “Preparation of novel ceramic membranes modified by mesoporous silica with 3-aminopropyltriethoxysilane (APTES) and its application to Cu^{2+} separation in the aqueous phase”, *Journal of Membrane Science* **2007**, *301*, 118-125.